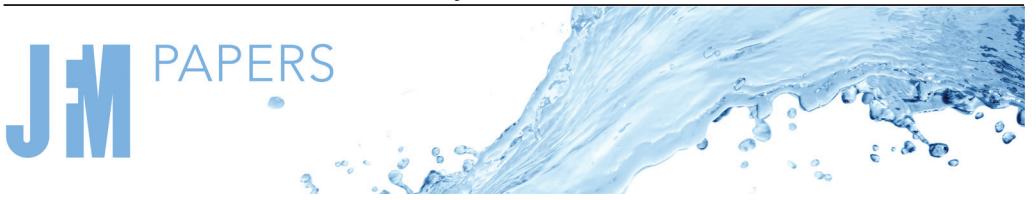
CrossMark

J. Fluid Mech. (2021), *vol*. 927, A25, doi:10.1017/jfm.2021.762



Structured input–output analysis of transitional wall-bounded flows

Chang Liu[1],† **and Dennice F. Gayme**[1]

[1]Department of Mechanical Engineering, Johns Hopkins University, Baltimore, MD 21218, USA

(Received 31 March 2021; revised 10 July 2021; accepted 22 August 2021)

Input–output analysis of transitional channel flows has proven to be a valuable analytical tool for identifying important flow structures and energetic motions. The traditional approach abstracts the nonlinear terms as forcing that is unstructured, in the sense that this forcing is not directly tied to the underlying nonlinearity in the dynamics. This paper instead employs a structured-singular-value-based approach that preserves certain input–output properties of the nonlinear forcing function in an effort to recover the larger range of key flow features identified through nonlinear analysis, experiments and direct numerical simulation (DNS) of transitional channel flows. Application of this method to transitional plane Couette and plane Poiseuille flows leads to not only the identification of the streamwise coherent structures predicted through traditional input–output approaches, but also the characterization of the oblique flow structures as those requiring the least energy to induce transition, in agreement with DNS studies, and nonlinear optimal perturbation analysis. The proposed approach also captures the recently observed oblique turbulent bands that have been linked to transition in experiments and DNS with very large channel size. The ability to identify the larger amplification of the streamwise varying structures predicted from DNS and nonlinear analysis in both flow regimes suggests that the structured approach allows one to maintain the nonlinear effects associated with weakening of the lift-up mechanism, which is known to dominate the linear operator. Capturing this key nonlinear effect enables the prediction of a wider range of known transitional flow structures within the analytical input–output modelling paradigm.

Key words: transition to turbulence

1. Introduction

Interest in transitional wall-bounded shear flow dates back to early studies by Reynolds (1883), who noted that the flow in a pipe was sensitive to disturbances. Though much progress has been made, a full understanding of the phenomena has yet to be realized.

† Email address for correspondence: changliu@jhu.edu

© The Author(s), 2021. Published by Cambridge University Press

https://doi.org/10.1017/jfm.2021.762 Published online by Cambridge University Press

One of the main challenges lies in the fact that linear stability analysis fails to accurately predict the Reynolds numbers at which flows are observed to transition to turbulence. For example, plane Couette flow is linearly stable for any Reynolds number (Romanov 1973) yet is observed to transition to turbulence at Reynolds numbers as low as 360 ± 10 (Tillmark & Alfredsson 1992). This failure has led researchers to study the mechanisms underlying transition by instead analysing energy growth. In particular, there has been an emphasis on characterizing the types of finite-amplitude perturbations that are most likely to lead to transition as well as the flow structures that dominate in this regime (e.g. Schmid & Henningson 1992; Lundbladh, Henningson & Reddy 1994; Reddy *et al.* 1998; Philip, Svizher & Cohen 2007; Duguet, Brandt & Larsson 2010*a*; Duguet *et al.* 2013; Farano *et al.* 2015).

Reddy *et al.* (1998) examined the relative flow response of different transition-inducing flow perturbations in both plane Couette flow and Poiseuille flow through extensive direct numerical simulations (DNS). Those authors observed that both streamwise vortices and oblique waves require less energy density than random noise to trigger transition (Reddy *et al.* 1998, figures 19 and 23) in both flows. They further showed that in Poiseuille flow even perturbations in the form of Tollmien–Schlichting (TS) waves, which are linearly unstable at $Re > 5772$ (Orszag 1971), require larger energy density to trigger transition than either streamwise vortices or oblique waves (Reddy *et al.* 1998, figure 19). Similar behaviour has been observed in studies of the transient energy growth and input–output response of the linearized Navier–Stokes (LNS) equations (Reddy & Henningson 1993; Jovanović & Bamieh 2005). In fact, input–output analysis of channel flow suggests that streamwise constant structures have larger energy growth than the linearly unstable TS waves, even at supercritical Reynolds numbers (i.e. above the Reynolds number at which the laminar flow is no longer linearly stable) (Jovanović 2004; Jovanović & Bamieh 2004). Studies of the LNS have indicated that streamwise vortical structures represent both the initial condition (optimal perturbation) that leads to the largest energy growth (Gustavsson 1991; Butler & Farrell 1992; Reddy & Henningson 1993; Schmid & Henningson 2001) as well as the type of structure that sustains the highest energy growth (e.g. Farrell & Ioannou 1993; Bamieh & Dahleh 2001; Jovanović & Bamieh 2005). The importance of streamwise vortices was also confirmed by Bottin *et al.* (1998), who connected experimental results with this form of exact coherent structures in plane Couette flow.

On the other hand, the simulations of Schmid & Henningson (1992) and Reddy *et al.* (1998) as well as the experiments of Elofsson & Alfredsson (1998) indicate that perturbations of oblique waves require slightly less energy than streamwise vortices to initiate transition. Nonlinear optimal perturbations (NLOP) to plane Couette flow, i.e. the initial perturbations that require the least energy to transition the flow from laminar to turbulent, also take the form of oblique waves that are localized in the streamwise direction (e.g. Duguet *et al.* 2010*a*, 2013; Monokrousos *et al.* 2011; Rabin, Caulfield & Kerswell 2012; Cherubini & De Palma 2013, 2015). For plane Poiseuille flow, hairpin vortices associated with the very short time scale of the Orr mechanism represent the NLOP (Farano *et al.* 2015, 2016). These results suggest that traditional linear analysis does not capture the full range of highly amplified structures in transitional flows.

Recent experiments and DNS of plane Couette flow with very large channel size ($\sim O(100)$ times the channel half-height) have also uncovered oblique turbulent bands (turbulent stripes) in the transitional flow regime of wall-bounded shear flows (e.g. Prigent *et al.* 2002, 2003; Duguet, Schlatter & Henningson 2010*b*; De Souza, Bergier & Monchaux 2020; Tuckerman, Chantry & Barkley 2020). These turbulent–laminar patterns were also

https://doi.org/10.1017/jfm.2021.762 Published online by Cambridge University Press

observed in DNS of transitional plane Poiseuille flow with sufficiently large channel size (Tsukahara *et al.* 2005; Xiong *et al.* 2015; Kanazawa 2018; Tao, Eckhardt & Xiong 2018; Shimizu & Manneville 2019; Song & Xiao 2020; Xiao & Song 2020). The presence of such structures was later confirmed by experiments (Hashimoto *et al.* 2009; Paranjape 2019; Paranjape, Duguet & Hof 2020, figure 1). There is strong evidence that the mechanisms leading to the growth and maintenance of these oblique turbulent bands are nonlinear in both plane Couette flow (Barkley & Tuckerman 2007; Tuckerman & Barkley 2011; Duguet & Schlatter 2013) and plane Poiseuille flow (Tuckerman *et al.* 2014). That view has been further supported by analysis of exact equilibrium and travelling wave solutions of the nonlinear Navier–Stokes (NS) equations (e.g. for plane Couette flow (Deguchi & Hall 2015; Reetz, Kreilos & Schneider 2019) and Poiseuille flow (Paranjape *et al.* 2020)).

The literature described above points to the benefit of nonlinear methods in characterizing the full range of flow structures in transitional channel flow. However, these methods have far larger computational costs than linear analysis methods (e.g. Kerswell, Pringle & Willis 2014; Kerswell 2018). This trade-off between obtaining a more comprehensive characterization of the phenomena and analysis that is computationally tractable is long-standing. However, there is significant evidence to suggest that insight can be gained through parametrizing or bounding the effect of the nonlinearity rather than undertaking the full computational burden of resolving it. For example, Kreiss, Lundbladh & Henningson (1994) and Chapman (2002) employed a bound on the nonlinearity to derive a finite-amplitude permissible perturbation that a flow could sustain while remaining laminar. More recently, finite-amplitude stability analysis of transitional shear flows employed local componentwise (sector) bounds on the nonlinearity and exploited the passivity of the nonlinear operator to develop linear-matrix-inequality-based approaches to compute bounds on permissible perturbations for a range of shear flow models (e.g. Kalur, Seiler & Hemati 2021*b*, 2020; Kalur *et al.* 2021*a*; Liu & Gayme 2020*b*). The inclusion of information about the nonlinear behaviour produced results that matched simulation data better than those derived through previous linear approaches. Data-driven methods to parametrize or colour (in space or time) the input (forcing) applied to the dynamics linearized around the turbulent mean velocity have also enabled nonlinear effects to be captured within the input–output framework, leading to better prediction of flow statistics (Chevalier *et al.* 2006; Zare, Jovanović & Georgiou 2017; Morra *et al.* 2021; Nogueira *et al.* 2021). The effect of the nonlinearity in the NS equations has also been incorporated directly into input–output and resolvent analysis through shaping or parametrizing the forcing, e.g. by including larger-amplitude forcing in the near-wall region (Jovanović & Bamieh 2001; Hœpffner *et al.* 2005).

In this work, we build on this notion of including the effect of the nonlinearity within a computationally tractable linear framework using the concept of a structured uncertainty (e.g. Packard & Doyle 1993; Zhou, Doyle & Glover 1996). In particular, we partition the NS equations into a feedback interconnection between the linearized dynamics and a model of the nonlinear forcing, as shown in figure 1. We then structure the feedback to enforce a block-diagonal structure (bottom block outlined by the blue dashed rectangle). In particular, the feedback defines the componentwise inputs to the linearized momentum equations, which are modelled in terms of an uncertain gain $-\boldsymbol{u}_\xi$ of an input–output mapping from each component ∇u, ∇v and ∇w to the respective forcings $f_{x,\xi}$, $f_{y,\xi}$ and $f_{z,\xi}$. We represent this gain using the structured singular value (Doyle 1982; Safonov 1982), μ, which we use to define the largest gain under the structured forcing (Packard & Doyle 1993). Conceptually the approach allows us to develop a feedback interconnection between

https://doi.org/10.1017/jfm.2021.762 Published online by Cambridge University Press

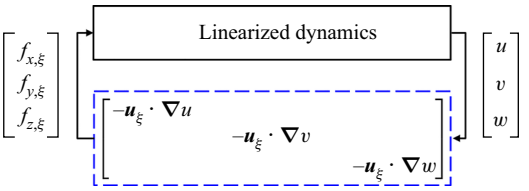


Figure 1. Block diagram representing the structured input–output feedback interconnection between the linearized dynamics and structured forcing modelling the nonlinearity (in the blue dashed region). In particular, each component of the forcing is modelled as an input–output mapping from the respective component of the velocity gradient ∇u, ∇v, ∇w to the respective component forcings $f_{x,\xi}, f_{y,\xi}, f_{z,\xi}$ of the linearized dynamics with the gain $-\boldsymbol{u}_\xi$ defined in terms of the structured singular value of a linearized closed-loop system response.

the LNS equations and a structured forcing that is explicitly constrained to preserve the componentwise structure of the nonlinearity in the NS equations.

Structured input–output analysis shares the advantages of all methods employing analysis of the spatio-temporal frequency response, which this work builds upon (e.g. Farrell & Ioannou 1993; Bamieh & Dahleh 2001; Jovanović & Bamieh 2005; McKeon & Sharma 2010; McKeon, Sharma & Jacobi 2013; McKeon 2017; Illingworth, Monty & Marusic 2018; Vadarevu *et al.* 2019; Madhusudanan, Illingworth & Marusic 2019; Symon, Illingworth & Marusic 2021; Liu & Gayme 2019, 2020*a*). Of greatest interest in this work is its computational tractability compared with nonlinear approaches and the lack of finite channel size effects that can plague both DNS and experimental studies. This approach is most closely related to the analysis of the largest singular value ($\mathcal{H}_\infty$ norm) of the spatio-temporal frequency response of the linearized dynamics (top block of figure 1), which measures the structure that sustains the highest input–output growth (e.g. Jovanović 2004; Schmid 2007; Hwang & Cossu 2010*a*,*b*; Illingworth 2020). However, in those works the forcing is assumed to excite the dynamics at all frequencies (e.g. delta-correlated spatio-temporal white noise); in this sense, it can be thought of as the open-loop response of the top block in figure 1.

We apply the proposed structured input–output analysis to transitional plane Couette and plane Poiseuille flows. The results indicate that the addition of a structured feedback interconnection enables identification and analysis of the wider range of transition-inducing flow structures identified in the literature without the computational burden of nonlinear optimization or extensive simulations. More specifically, the results for transitional plane Couette flow reproduce results from DNS-based analysis (Reddy *et al.* 1998) and predictions of NLOP approaches (Rabin *et al.* 2012), which both indicate that oblique waves require less energy to induce transition than the streamwise elongated structures emphasized in traditional input–output analysis. In plane Poiseuille flow, these transition-inducing flow structures are consistent with DNS (Reddy *et al.* 1998) emphasizing oblique waves and NLOP analysis that highlights the importance of spatially localized structures with streamwise wavelengths larger than their spanwise extent (Farano *et al.* 2015). The proposed approach also reproduces the characteristic wavelengths and angle of the oblique turbulent band observed in very-large-channel studies of transitional plane Couette flow (Prigent *et al.* 2003). The wavelengths of oblique turbulent bands in transitional plane Poiseuille flow with very large channel size (Kanazawa 2018) also fall within the range of flow structures showing large structured input–output response.

The agreement between predictions from structured input–output analysis and observations from experiments, DNS and NLOP analysis show that this framework

https://doi.org/10.1017/jfm.2021.762 Published online by Cambridge University Press

captures important nonlinear effects. In particular, the results suggest that restricting the feedback in a componentwise manner preserves the structure of the nonlinear mechanisms that weaken the streaks developed through the lift-up effect, in which cross-stream forcing amplifies streamwise streaks (Ellingsen & Palm 1975; Landahl 1975; Brandt 2014). Traditional input–output analysis instead predicts the dominance of streamwise elongated structures associated with the lift-up mechanism (see e.g. the discussion in Jovanović (2021)). An examination of Reynolds number trends supports the notion that imposing a structured feedback interconnection based on certain input–output properties associated with the nonlinearity in the NS equations leads to a weakening of the amplification of streamwise elongated structures.

The remainder of this paper is organized as follows. Section 2 describes the flow configurations of interest and the details of the structured input–output analysis approach. Section 3 analyses the results obtained from the application of structured input–output analysis to both plane Couette flow and plane Poiseuille flow. We then analyse Reynolds number dependence in § 4. The paper is concluded in § 5.

2. Formulating the structured input–output model

2.1. *Governing equations*

We consider incompressible flow between two infinite parallel plates and employ x, y and z to respectively denote the streamwise, wall-normal and spanwise directions. The corresponding velocity components are denoted by u, v and w. The coordinate frames and configurations used for plane Couette flow and plane Poiseuille flow are shown in figure 2. We express the velocity field as a vector $\boldsymbol{u}_{tot} = [u_{tot}\ v_{tot}\ w_{tot}]^{\mathrm{T}}$ with superscript 'T' indicating the transpose. We then decompose the velocity field into the sum of a laminar base flow ($U(y) = y$ for plane Couette flow and $U(y) = 1 - y^2$ for plane Poiseuille flow) and fluctuations about the base flow $\boldsymbol{u}$; i.e. $\boldsymbol{u}_{tot} = U(y)\boldsymbol{e}_x + \boldsymbol{u}$ with $\boldsymbol{e}_x$ denoting the x direction (streamwise) unit vector. The pressure field is similarly decomposed into $p_{tot} = P + p$. The dynamics of the fluctuations $\boldsymbol{u}$ and p is governed by the NS equations:

$$\partial_t \boldsymbol{u} + U\partial_x \boldsymbol{u} + v\frac{dU}{\mathrm{d}y}\boldsymbol{e}_x + \boldsymbol{\nabla} p - \frac{1}{Re}\nabla^2 \boldsymbol{u} = -\boldsymbol{u}\cdot\boldsymbol{\nabla}\boldsymbol{u}, \tag{2.1a}$$

$$\boldsymbol{\nabla}\cdot\boldsymbol{u} = 0. \tag{2.1b}$$

Here, the spatial variables are normalized by the channel half-height h: e.g. $y = y_*/h \in [-1, 1]$, where the subscript $*$ indicates dimensional quantities. The velocity is normalized by a nominal characteristic velocity U_n, where $\pm U_n$ is the velocity at the channel walls for plane Couette flow and U_n is the channel centreline velocity for plane Poiseuille flow. Time and pressure are normalized by h/U_n and ρU_n^2, respectively. The Reynolds number is defined as $Re = U_n h/\nu$, where ν is the kinematic viscosity. In (2.1), $\boldsymbol{\nabla} := \begin{bmatrix}\partial_x & \partial_y & \partial_z\end{bmatrix}^{\mathrm{T}}$ represents the gradient operator and $\nabla^2 := \partial_x^2 + \partial_y^2 + \partial_z^2$ represents the Laplacian operator. We impose no-slip boundary conditions at the wall; i.e. $\boldsymbol{u}(y = \pm 1) = \boldsymbol{0}$ for both flows. Finally, we write the nonlinear term in (2.1*a*) as

$$\boldsymbol{f} := -\boldsymbol{u}\cdot\boldsymbol{\nabla}\boldsymbol{u} = [-\boldsymbol{u}\cdot\boldsymbol{\nabla}u \quad -\boldsymbol{u}\cdot\boldsymbol{\nabla}v \quad -\boldsymbol{u}\cdot\boldsymbol{\nabla}w]^{\mathrm{T}} =: \begin{bmatrix}f_x & f_y & f_z\end{bmatrix}^{\mathrm{T}}, \tag{2.2}$$

where =: indicates that the right-hand side is defined by the left-hand side. We refer to f_x, f_y and f_z as the respective streamwise, wall-normal and spanwise components of the nonlinearity and collectively as the nonlinear components of (2.1). This expression of the

https://doi.org/10.1017/jfm.2021.762 Published online by Cambridge University Press

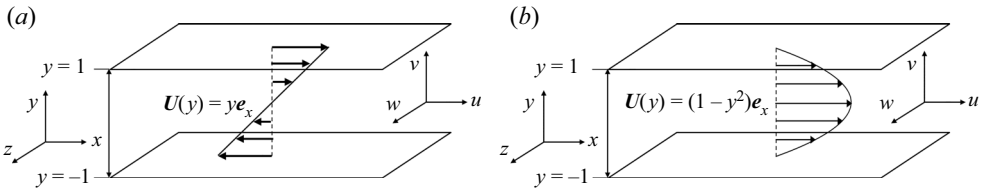


Figure 2. Illustrations of flows between two parallel flat plates: (*a*) plane Couette flow with laminar base flow $\boldsymbol{U}(y) = y\boldsymbol{e}_x$ and (*b*) plane Poiseuille flow with laminar base flow $\boldsymbol{U}(y) = (1 - y^2)\boldsymbol{e}_x$.

nonlinearity as forcing terms makes (2.1) into a set of forced linear evolution equations. This approach builds on the growing body of work that has shown promise in capturing critical features of this forced system response using linear analysis techniques (see e.g. the reviews of Schmid (2007), McKeon (2017) and Jovanović (2021) and references therein).

We next construct the model of the nonlinearity that will allow us to build the feedback interconnection of figure 1. The velocity field $-\boldsymbol{u}$ in (2.2) associated with the forcing components can be viewed as the gain operator of an input–output system in which the velocity gradients ∇u, ∇v and ∇w act as the respective inputs and the forcing components f_x, f_y and f_z act as the respective outputs. It is this gain that we seek to model through $-\boldsymbol{u}_\xi$ in figure 1. This input–output model of the nonlinear components is given by

$$\boldsymbol{f}_\xi := -\boldsymbol{u}_\xi \cdot \nabla \boldsymbol{u} = [-\boldsymbol{u}_\xi \cdot \nabla u \quad -\boldsymbol{u}_\xi \cdot \nabla v \quad -\boldsymbol{u}_\xi \cdot \nabla w]^{\mathrm{T}} =: \begin{bmatrix} f_{x,\xi} & f_{y,\xi} & f_{z,\xi} \end{bmatrix}^{\mathrm{T}}, \tag{2.3}$$

where $-\boldsymbol{u}_\xi = [-u_\xi, -v_\xi, -w_\xi]^{\mathrm{T}}$ maps the corresponding velocity gradient into each component of the modelled forcing driving the linearized dynamics. The next subsection describes how we construct this input–output map so that it enables us to analyse the perturbations that are most likely to induce transition using the structured singular value formalism (Packard & Doyle 1993; Zhou *et al.* 1996).

2.2. *Structured input–output response*

We now define the spatio-temporal frequency response $\mathcal{H}_\nabla(y; k_x, k_z, \omega)$ that will form the basis of the structured input–output response. We first perform the standard transformation to express the dynamics (2.1) in terms of the wall-normal velocity v and wall-normal vorticity $\omega_y := \partial_z u - \partial_x w$ (Schmid & Henningson 2001), which enforces (2.1*b*) and eliminates the pressure dependence. This formulation similarly imposes the divergence-free condition on the forcing model, since any component of the input forcing that can be written as the gradient of a scalar function $\boldsymbol{f}_\phi = \nabla\phi$ will be absorbed into the pressure gradient and eliminated. We then exploit the shift-invariance in the (x, z) spatial directions of the two flow configurations of interest and assume invariance to shifts in t, which allows us to perform the following triple Fourier transform for a variable ψ:

$$\hat{\psi}(y; k_x, k_z, \omega) := \int_{-\infty}^{\infty}\int_{-\infty}^{\infty}\int_{-\infty}^{\infty} \psi(x, y, z, t) \exp(-\mathrm{i}(k_x x + k_z z + \omega t))\, \mathrm{d}x\, \mathrm{d}z\, \mathrm{d}t, \tag{2.4}$$

where $\mathrm{i} = \sqrt{-1}$ is the imaginary unit, ω is the temporal frequency and $k_x = 2\pi/\lambda_x$ and $k_z = 2\pi/\lambda_z$ are the respective dimensionless x and z wavenumbers.

https://doi.org/10.1017/jfm.2021.762 Published online by Cambridge University Press

The resulting system of equations describing the transformed linearized equations subject to the modelled forcing $\boldsymbol{f}_\xi$ is

$$\mathrm{i}\omega \begin{bmatrix} \hat{v} \\ \hat{\omega}_y \end{bmatrix} = \hat{\mathcal{A}} \begin{bmatrix} \hat{v} \\ \hat{\omega}_y \end{bmatrix} + \hat{\mathcal{B}} \begin{bmatrix} \hat{f}_{x,\xi} \\ \hat{f}_{y,\xi} \\ \hat{f}_{z,\xi} \end{bmatrix}, \quad \begin{bmatrix} \hat{u} \\ \hat{v} \\ \hat{w} \end{bmatrix} = \hat{\mathcal{C}} \begin{bmatrix} \hat{v} \\ \hat{\omega}_y \end{bmatrix}. \tag{2.5a,b}$$

The operators in (2.5) are defined following Jovanović & Bamieh (2005):

$$\hat{\mathcal{A}}(k_x, k_z) := \begin{bmatrix} \hat{\nabla}^2 & 0 \\ 0 & \mathcal{I} \end{bmatrix}^{-1} \begin{bmatrix} -\mathrm{i}k_x U \hat{\nabla}^2 + \mathrm{i}k_x U'' + \hat{\nabla}^4/Re & 0 \\ -\mathrm{i}k_z U' & -\mathrm{i}k_x U + \hat{\nabla}^2/Re \end{bmatrix}, \tag{2.6a}$$

$$\hat{\mathcal{B}}(k_x, k_z) := \begin{bmatrix} \hat{\nabla}^2 & 0 \\ 0 & \mathcal{I} \end{bmatrix}^{-1} \begin{bmatrix} -\mathrm{i}k_x \partial_y & -(k_x^2 + k_z^2) & -\mathrm{i}k_z \partial_y \\ \mathrm{i}k_z & 0 & -\mathrm{i}k_x \end{bmatrix}, \tag{2.6b}$$

$$\hat{\mathcal{C}}(k_x, k_z) := \frac{1}{k_x^2 + k_z^2} \begin{bmatrix} \mathrm{i}k_x \partial_y & -\mathrm{i}k_z \\ k_x^2 + k_z^2 & 0 \\ \mathrm{i}k_z \partial_y & \mathrm{i}k_x \end{bmatrix}, \tag{2.6c}$$

where $U' := \mathrm{d}U(y)/\mathrm{d}y$, $U'' := \mathrm{d}^2U(y)/\mathrm{d}y^2$, $\hat{\nabla}^2 := \partial_{yy} - k_x^2 - k_z^2$ and $\hat{\nabla}^4 := \partial_y^{(4)} - 2(k_x^2 + k_z^2)\partial_{yy} + (k_x^2 + k_z^2)^2$. The boundary conditions, which can be derived from the no-slip conditions, are

$$\hat{v}(y = \pm 1) = \frac{\partial \hat{v}}{\partial y}(y = \pm 1) = \hat{\omega}_y(y = \pm 1) = 0. \tag{2.7}$$

The spatio-temporal frequency response $\mathcal{H}$ of the system in (2.5) that maps the input forcing $\hat{\boldsymbol{f}}_\xi(y; k_x, k_z, \omega)$ to the velocity vector $\hat{\boldsymbol{u}}(y; k_x, k_z, \omega)$ at the same spatio-temporal wavenumber–frequency triplet, i.e. $\hat{\boldsymbol{u}}(y; k_x, k_z, \omega) = \mathcal{H}(y; k_x, k_z, \omega)\hat{\boldsymbol{f}}_\xi(y; k_x, k_z, \omega)$, is given by

$$\mathcal{H}(y; k_x, k_z, \omega) := \hat{\mathcal{C}}(\mathrm{i}\omega \mathcal{I}_{2\times 2} - \hat{\mathcal{A}})^{-1}\hat{\mathcal{B}}. \tag{2.8}$$

Here $\mathcal{I}_{2\times 2} := \mathrm{diag}(\mathcal{I}, \mathcal{I})$, where $\mathcal{I}$ is the identity operator and $\mathrm{diag}(\cdot)$ indicates a block diagonal operation. Following the language in Jovanović (2021), we also refer to $\mathcal{H}(y; k_x, k_y, \omega)$ defined in (2.8) as the frequency response operator.

The linear form of (2.3) allows us to also perform the spatio-temporal Fourier transform (2.4) on this forcing model to obtain

$$\hat{\boldsymbol{f}}_\xi = -\hat{\boldsymbol{u}}_\xi \cdot \hat{\boldsymbol{\nabla}}\hat{\boldsymbol{u}} = \begin{bmatrix} \hat{f}_{x,\xi} \\ \hat{f}_{y,\xi} \\ \hat{f}_{z,\xi} \end{bmatrix} = \begin{bmatrix} -\hat{\boldsymbol{u}}_\xi^{\mathrm{T}} & & \\ & -\hat{\boldsymbol{u}}_\xi^{\mathrm{T}} & \\ & & -\hat{\boldsymbol{u}}_\xi^{\mathrm{T}} \end{bmatrix} \begin{bmatrix} \hat{\boldsymbol{\nabla}}\hat{u} \\ \hat{\boldsymbol{\nabla}}\hat{v} \\ \hat{\boldsymbol{\nabla}}\hat{w} \end{bmatrix}, \tag{2.9}$$

which can be decomposed as

$$\begin{bmatrix} \hat{f}_{x,\xi} \\ \hat{f}_{y,\xi} \\ \hat{f}_{z,\xi} \end{bmatrix} = \mathrm{diag}\left(-\hat{\boldsymbol{u}}_\xi^{\mathrm{T}}, -\hat{\boldsymbol{u}}_\xi^{\mathrm{T}}, -\hat{\boldsymbol{u}}_\xi^{\mathrm{T}}\right) \mathrm{diag}\left(\hat{\boldsymbol{\nabla}}, \hat{\boldsymbol{\nabla}}, \hat{\boldsymbol{\nabla}}\right) \begin{bmatrix} \hat{u} \\ \hat{v} \\ \hat{w} \end{bmatrix}. \tag{2.10}$$

This decomposition of the forcing function is illustrated in the two blocks inside the blue dashed region in figure 3(*a*), where the velocity field arising from the spatio-temporal frequency response $\mathcal{H}$ is the input and the forcing is the output.

https://doi.org/10.1017/jfm.2021.762 Published online by Cambridge University Press

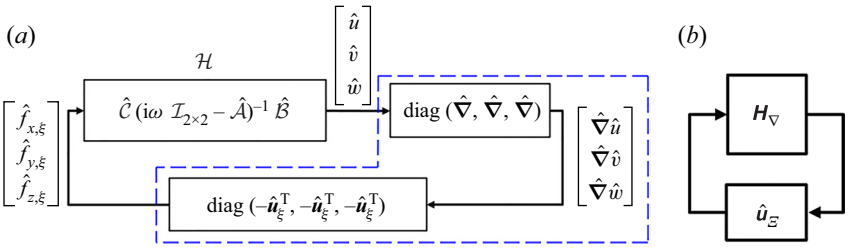


Figure 3. Illustration of feedback interconnection associated with structured input–output analysis: (*a*) a componentwise description, where blocks inside of the blue dashed region represent the modelled forcing in (2.10) corresponding to the bottom block of figure 1; (*b*) a high-level description after discretization.

In order to isolate the gain $-\boldsymbol{u}_\xi$ that we seek to model, it is analytically convenient to combine the linear gradient operator with the spatio-temporal frequency response. The resulting modified frequency response operator is

$$\mathcal{H}_\nabla(y; k_x, k_z, \omega) := \mathrm{diag}(\hat{\boldsymbol{\nabla}}, \hat{\boldsymbol{\nabla}}, \hat{\boldsymbol{\nabla}})\mathcal{H}(y; k_x, k_z, \omega). \tag{2.11}$$

We note that this operator in (2.11) can be also obtained by modifying $\hat{\mathcal{C}}$ in (2.8) such that the output corresponds to a vectorized velocity gradient. Finally, we redraw the system as a feedback interconnection between this linear operator in (2.11) and the structured uncertainty

$$\hat{\boldsymbol{u}}_\Xi := \mathrm{diag}\left(-\hat{\boldsymbol{u}}_\xi^{\mathrm{T}}, -\hat{\boldsymbol{u}}_\xi^{\mathrm{T}}, -\hat{\boldsymbol{u}}_\xi^{\mathrm{T}}\right). \tag{2.12}$$

The structured uncertainty $\hat{\boldsymbol{u}}_\Xi$ in (2.12) has a block-diagonal structure such that the resulting feedback interconnection leads to a forcing model that retains the componentwise structure of the nonlinearity. Figure 3(*b*) describes the resulting feedback interconnection between the modified spatio-temporal frequency response and the structured uncertainty, where $\boldsymbol{H}_\nabla$ and $\hat{\boldsymbol{u}}_\Xi$ respectively represent the spatial discretizations (numerical approximations) of $\mathcal{H}_\nabla$ in (2.11) and $\hat{\boldsymbol{u}}_\Xi$ in (2.12).

We are interested in characterizing the perturbations associated with the most amplified flow structures under structured forcing. This amplification under structured forcing can be quantified by the structured singular value of the modified frequency response operator $\mathcal{H}_\nabla$ (see e.g. Packard & Doyle (1993, definition 3.1) and Zhou *et al.* (1996, definition 11.1)), which is defined as follows.

DEFINITION 2.1. *Given wavenumber and frequency pair* (k_x, k_z, ω)*, the structured singular value* $\mu_{\hat{\boldsymbol{U}}_\Xi}[\boldsymbol{H}_\nabla(k_x, k_z, \omega)]$ *is defined as*

$$\mu_{\hat{\boldsymbol{U}}_\Xi}[\boldsymbol{H}_\nabla(k_x, k_z, \omega)] := \frac{1}{min\{\bar{\sigma}[\hat{\boldsymbol{u}}_\Xi]\ :\ \hat{\boldsymbol{u}}_\Xi \in \hat{\boldsymbol{U}}_\Xi,\ det[\boldsymbol{I} - \boldsymbol{H}_\nabla(k_x, k_z, \omega)\hat{\boldsymbol{u}}_\Xi] = 0\}}, \tag{2.13}$$

unless no $\hat{\boldsymbol{u}}_\Xi \in \hat{\boldsymbol{U}}_\Xi$ *makes* $\boldsymbol{I} - \boldsymbol{H}_\nabla\hat{\boldsymbol{u}}_\Xi$ *singular, in which case* $\mu_{\hat{\boldsymbol{U}}_\Xi}[\boldsymbol{H}_\nabla] := 0$.

Here, $\bar{\sigma}[\cdot]$ *is the largest singular value,* $det[\cdot]$ *is the determinant of the argument and* $\boldsymbol{I}$ *is the identity matrix. The subscript of* μ *in (2.13) is a set* $\hat{\boldsymbol{U}}_\Xi$ *containing all uncertainties having the same block-diagonal structure as* $\hat{\boldsymbol{u}}_\Xi$*; i.e.*

$$\hat{\boldsymbol{U}}_\Xi := \{diag(-\hat{\boldsymbol{u}}_\xi^T, -\hat{\boldsymbol{u}}_\xi^T, -\hat{\boldsymbol{u}}_\xi^T) : -\hat{\boldsymbol{u}}_\xi^T \in \mathbb{C}^{N_y\times 3N_y}\}, \tag{2.14}$$

where N_y *denotes the number of grid points in* y.

https://doi.org/10.1017/jfm.2021.762 Published online by Cambridge University Press

For ease of computation and analysis, the form of the structured uncertainty in (2.14) allows the full degrees of freedom for the complex matrix $-\hat{\boldsymbol{u}}_\xi^{\mathrm{T}} \in \mathbb{C}^{N_y \times 3N_y}$. A natural refinement to better represent the physics would be to enforce a diagonal structure for each of the sub-blocks of this matrix. This approach is not pursued here because it requires extensions of both the analysis and computational tools to properly evaluate the response. These extensions are beyond the scope of the current work.

The largest structured singular value across all temporal frequencies characterizes the largest response associated with a stable structured feedback interconnection (i.e. the full block diagram in figure 3*b*). Here, stability is defined in terms of the small gain theorem (Zhou *et al.* 1996, theorem 11.8).

PROPOSITION 2.2 (small gain theorem). *Given* $0 < \beta < \infty$ *and wavenumber pair* (k_x, k_z). *The loop shown in figure 3(b) is stable for all* $\hat{\boldsymbol{u}}_\Xi \in \hat{\boldsymbol{U}}_\Xi$ *with* $\|\hat{\boldsymbol{u}}_\Xi\|_\infty := \sup_{\omega\in\mathbb{R}} \bar{\sigma}[\hat{\boldsymbol{u}}_\Xi] < 1/\beta$ *if and only if:*

$$\|\mathcal{H}_\nabla\|_\mu(k_x, k_z) := \sup_{\omega\in\mathbb{R}} \mu_{\hat{\boldsymbol{U}}_\Xi}[\boldsymbol{H}_\nabla(k_x, k_z, \omega)] \leqslant \beta. \tag{2.15}$$

Here, sup represents supremum (least upper bound) operation, and we abuse the notation by writing $\|\cdot\|_\mu$ (Packard & Doyle 1993), although the quantity in (2.15) is not a proper norm (i.e. it does not necessarily satisfy the triangle inequality). This value $\|\mathcal{H}_\nabla\|_\mu(k_x, k_z)$ in (2.15) directly quantifies most amplified flow structures (characterized by the associated (k_x, k_z) pair) under structured forcing. This quantity is closely related to that obtained from input–output analysis based on the $\mathcal{H}_\infty$ norm (Jovanović 2004; Schmid 2007; Illingworth 2020) and characterizations of transient growth (e.g. Schmid 2007), where flow structures with high amplification under external input forcing or high transient energy growth are associated with transition.

2.3. *Numerical method*

The operators in (2.6) are discretized using the Chebyshev differentiation matrices generated by the MATLAB routines of Weideman & Reddy (2000). The boundary conditions in (2.7) are implemented following Trefethen (2000, chapters 7 and 14). We employ the Clenshaw–Curtis quadrature (Trefethen 2000, chapter 12) in computing both singular and structured singular values to ensure that they are independent of the number of Chebyshev spaced wall-normal grid points. The numerical implementation of the operators is validated through comparisons of the plane Poiseuille flow results for computations of the $\mathcal{H}_\infty$ norm in Jovanović (2004, chapter 8.1.2) and Schmid (2007, figure 5), and plane Couette flow in Jovanović (2004, chapter 8.2). We use $N_y = 30$ collocation points (excluding the boundary points), which is the same number employed in Jovanović & Bamieh (2005) and Jovanović (2004). We verified that doubling the number of collocation points in the wall-normal direction does not alter the results, indicating grid convergence. We employ, respectively, 50 and 90 logarithmically spaced points in the spectral range $k_x \in [10^{-4}, 10^{0.48}]$ and $k_z \in [10^{-2}, 10^{1.2}]$ which is similar to the numbers of points and ranges employed in Jovanović & Bamieh (2005).

We compute $\|\mathcal{H}_\nabla\|_\mu$ in (2.15) for each wavenumber pair (k_x, k_z) using the `mussv` command in the Robust Control Toolbox (Balas *et al.* 2005) of MATLAB R2020a. The arguments of `mussv` employed here include the state-space model of $\boldsymbol{H}_\nabla$ that samples the frequency domain adaptively. (The command `mussv` can adaptively sample frequency domain $\omega \in \mathbb{R}^+$, and the frequency domain $\omega \in \mathbb{R}^-$ can be computed by modifying the state-space model.) The `BlockStructure` argument comprises three full $N_y \times 3N_y$ complex

https://doi.org/10.1017/jfm.2021.762 Published online by Cambridge University Press

matrices, and we use the 'Uf' algorithm option. The average computation time for each wavenumber pair (k_x, k_z) is around 11 s on a computer with a 3.4 GHz Intel Core i7-3770 CPU and 16 GB RAM. These computations can be easily parallelized over either the k_x or k_z domain using, for example, the parfor command in the Parallel Computing Toolbox in MATLAB.

3. Structured spatio-temporal frequency response

In this section, we use $\|\mathcal{H}_\nabla\|_\mu(k_x, k_z)$ in (2.15) to characterize the flow structures (i.e. the (k_x,k_z) wavenumber pairs) that are most amplified in transitional plane Couette flow and plane Poiseuille flow. In order to illustrate the relative effect of the feedback interconnection versus the imposed structure we compare the results with

$$\|\mathcal{H}\|_\infty(k_x, k_z) := \sup_{\omega\in\mathbb{R}} \bar{\sigma}[\boldsymbol{H}(k_x, k_z, \omega)], \tag{3.1}$$

where $\boldsymbol{H}$ is the discretization of spatio-temporal frequency response operator $\mathcal{H}$ in (2.8). This quantity, which was previously analysed for transitional flows (Jovanović 2004; Schmid 2007; Illingworth 2020), describes the maximum singular value of the frequency response operator $\mathcal{H}$. This quantity represents the maximal gain of $\mathcal{H}$ over all temporal frequencies, i.e. the worst-case amplification over harmonic inputs. Therefore the highest values of $\|\mathcal{H}\|_\infty$ correspond to structures that are most amplified but not those with the largest sustained energy density that is often reported in the literature (e.g. Farrell & Ioannou 1993; Bamieh & Dahleh 2001; Jovanović & Bamieh 2005).

In order to isolate the effect of the structure imposed on the nonlinearity from the effect of the closed-loop feedback interconnection, we also compute

$$\|\mathcal{H}_\nabla\|_\infty(k_x, k_z) := \sup_{\omega\in\mathbb{R}} \bar{\sigma}[\boldsymbol{H}_\nabla(k_x, k_z, \omega)]. \tag{3.2}$$

This quantity is the unstructured counterpart of $\|\mathcal{H}_\nabla\|_\mu$, which is obtained by replacing the uncertainty set $\hat{\boldsymbol{U}}_\Xi$ with the set of full complex matrices $\mathbb{C}^{3N_y\times 9N_y}$ (Packard & Doyle 1993; Zhou *et al.* 1996). In other words, the definition does not specify a particular feedback pathway associated with each component of forcing, which leads to an unstructured feedback interconnection. We note that by definition $\|\mathcal{H}_\nabla\|_\mu(k_x, k_z) \leqslant \|\mathcal{H}_\nabla\|_\infty(k_x, k_z)$ (Packard & Doyle 1993, equation (3.4)). Comparisons between $\|\mathcal{H}_\nabla\|_\mu$ and $\|\mathcal{H}_\nabla\|_\infty$, therefore, highlight the effect of the structured uncertainty. The values $\|\mathcal{H}\|_\infty$ in (3.1) and $\|\mathcal{H}_\nabla\|_\infty$ in (3.2) are computed using the hinfnorm command in the Robust Control Toolbox (Balas *et al.* 2005) of MATLAB.

In the next subsection we analyse plane Couette flow at $Re = 358$. This is followed by a study of plane Poiseuille flow at $Re = 690$ in § 3.2. These Reynolds numbers are within the ranges of $Re \in [340, 393]$ and $Re \in [660, 720]$, where oblique turbulent bands are respectively observed in plane Couette flow (Prigent *et al.* 2003) and plane Poiseuille flow (Kanazawa 2018). These particular values were selected because there are data from previous studies (Prigent *et al.* 2003; Kanazawa 2018) available for comparison. This § 3.3 ends with a discussion of the role of the componentwise structure of the feedback interconnection in structured input–output analysis.

3.1. *Plane Couette flow at Re = 358*

In this subsection, we use the proposed approach to analyse the perturbations that are most likely to trigger transition in plane Couette flow at $Re = 358$ using the $\|\mathcal{H}_\nabla\|_\mu$

https://doi.org/10.1017/jfm.2021.762 Published online by Cambridge University Press

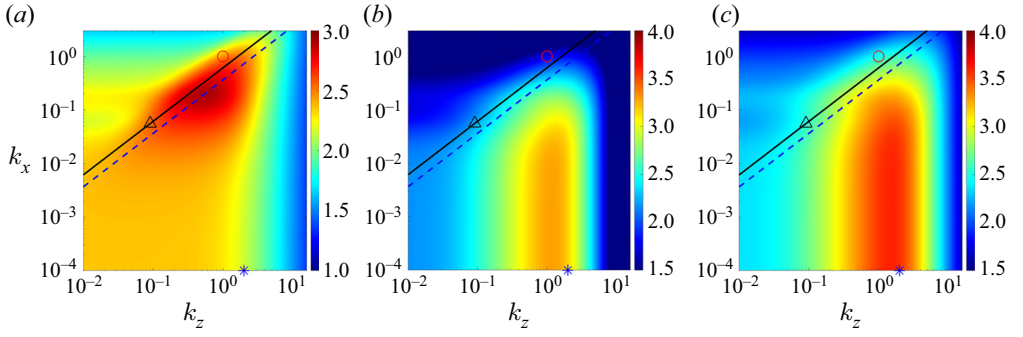


Figure 4. Contour plots of (*a*) $\log_{10}[\|\mathcal{H}_\nabla\|_\mu(k_x, k_z)]$, (*b*) $\log_{10}[\|\mathcal{H}\|_\infty(k_x, k_z)]$ and (*c*) $\log_{10}[\|\mathcal{H}_\nabla\|_\infty(k_x, k_z)]$ for plane Couette flow at $Re = 358$. Here the blue star indicates streamwise vortices with $k_x \approx 0$, $k_z = 2$; the red circle marks oblique waves with $k_x = k_z = 1$ as studied by (Reddy *et al.* 1998). The black triangle marks $\lambda_x = 113$, $\lambda_z = 69$ which are the observed wavelengths of the oblique turbulent band at $Re = 358$ (Prigent *et al.* 2003). The black solid line is $\lambda_z = \lambda_x \tan(32^\circ)$ representing a 32° angle of the oblique turbulent band, and the blue dashed line represents $\lambda_z = \lambda_x \tan(20^\circ)$.

formulation described in the previous section. Figure 4(*a*) shows this quantity alongside results obtained using input–output analysis describing the most amplified flow structures in terms of $\|\mathcal{H}\|_\infty$ in figure 4(*b*) and $\|\mathcal{H}_\nabla\|_\infty$ in (3.2) in figure 4(*c*). In all panels, we indicate the structures with $k_x \approx 0$ and $k_z = 2$ representing streamwise vortices using blue stars and indicate $k_x = 1$ and $k_z = 1$ representing the oblique waves that were observed as the structures requiring the least energy to trigger transition in the DNS of Reddy *et al.* (1998) using red circles. In general, the wavenumber pair $k_x \approx 0$ and $k_z = 2$ marked by blue stars represents streamwise elongated flow structures that include both streamwise vortices and streamwise streaks. However, we refer to $(k_x \approx 0, k_z = 2)$ as streamwise vortices when comparing with the results in Reddy *et al.* (1998) because that work explicitly introduced streamwise vortices associated with this wavenumber pair. Figure 4 shows clear differences in the dominant structures identified using the structured input–output approach. The largest magnitudes of $\|\mathcal{H}_\nabla\|_\mu$ in figure 4(*a*) are associated with oblique waves with $k_x \in [10^{-2}, 1]$ and $k_z \in [10^{-1}, 1]$, while the streamwise elongated structures that are dominant in figure 4(*b*,*c*) have a lesser but still large magnitude. This result is consistent with findings of Reddy *et al.* (1998, figure 23) showing that oblique waves require less perturbation energy to trigger turbulence in plane Couette flow than streamwise vortices. A comparison of $\|\mathcal{H}_\nabla\|_\infty$ in figure 4(*c*) and $\|\mathcal{H}\|_\infty$ in figure 4(*b*) indicates that it is not the feedback interconnection that significantly changes the dominant flow structures but rather the imposition of the componentwise structure of the nonlinearity. In addition, we observe that the magnitude of $\|\mathcal{H}_\nabla\|_\mu$ in figure 4(*a*) is lower than that of $\|\mathcal{H}_\nabla\|_\infty$ in figure 4(*c*) for each (k_x, k_z) pair, which is consistent with the fact that the unstructured gain $\|\mathcal{H}_\nabla\|_\infty$ provides an upper bound on the structured one, $\|\mathcal{H}_\nabla\|_\mu$ (Packard & Doyle 1993).

The difference between the results in figure 4 mirrors the differences between the optimal perturbation structures predicted by linear optimal perturbation and NLOP analyses. In particular, the structures predicted using $\|\mathcal{H}_\nabla\|_\mu$ are streamwise localized oblique waves reminiscent of those obtained as NLOP of plane Couette flow (Monokrousos *et al.* 2011; Duguet *et al.* 2010*a*, 2013; Rabin *et al.* 2012; Cherubini & De Palma 2013, 2015), whereas the results obtained using $\|\mathcal{H}\|_\infty$ in figure 4(*b*) indicate the dominance of the types of streamwise elongated flow structures predicted

https://doi.org/10.1017/jfm.2021.762 Published online by Cambridge University Press

as linear optimal perturbations (Butler & Farrell 1992). Our results also reflect previous findings that the NLOP is wider in the spanwise direction than the linear optimal perturbation (Rabin *et al.* 2012, figure 11). The results in figure 4 therefore indicate that the proposed structured input–output framework provides closer agreement with both DNS- and NLOP-based predictions of perturbations to which the flow is most sensitive than traditional input–output methods focusing on the spatio-temporal frequency response $\mathcal{H}$ in (2.8). The inclusion of a feedback loop for $\|\mathcal{H}_\nabla\|_\infty$ in figure 4(*c*) does lead to small improvements in the width of the structures predicted, but it does not lead to identification of the dominance of the oblique waves. This behaviour suggests that the weakening of the amplification of the streamwise elongated structures is a direct result of the structure imposed in the feedback interconnection.

Oblique turbulent bands have also been observed to be prominent in the transitional regime of plane Couette flow with very large channel size (Prigent *et al.* 2003; Duguet *et al.* 2010*b*). Figure 4 indicates the wavelength pair $\lambda_x = 113$ and $\lambda_z = 69$ (black triangle) associated with the oblique turbulent bands that are observed to have horizontal extents in the range $\lambda_x \in [107, 118]$ and $\lambda_z \in [62, 76]$ in very-large-channel studies of plane Couette flow at $Re = 358$; see Prigent *et al.* (2003, figures 3(*b*) and 5). The characteristic inclination angle measured from the streamwise direction in the x–z plane is $\theta := \tan^{-1}(\lambda_z/\lambda_x) = \tan^{-1}(69/113) \approx 32^\circ$. This value is indicated by the black solid line, $\lambda_z = \lambda_x \tan(32^\circ)$, in figure 4 and falls within the mid-range of the angles $\theta \in [28^\circ, 35^\circ]$ corresponding to the spread of the data in Prigent *et al.* (2003, figure 5). Other simulations employing a tilted domain to impose an angle constrained by periodic boundary conditions in the streamwise and spanwise directions indicate that the oblique turbulent bands can be maintained by an angle as low as 20°; see e.g. Duguet *et al.* (2010*b*, figure 6). In figure 4, we also plot the angle 20° represented by the blue dashed line, $\lambda_z = \lambda_x \tan(20^\circ)$, which is shown to correspond to the centre of the peak region of $\|\mathcal{H}_\nabla\|_\mu$. The results in the literature indicate that oblique structures associated with a range of wavelengths and inclination angles may provide large amplification, which may be the reason for the large peak region of $\|\mathcal{H}_\nabla\|_\mu$ in figure 4(*a*). These results suggest that structured input–output analysis captures the angle of the oblique turbulent band in transitional plane Couette flow. While there is some footprint of these types of structures in all three panels, the ranges of characteristic wavelengths and angles are most clearly associated with the peak region of $\|\mathcal{H}_\nabla\|_\mu$ in figure 4(*a*), and the line representing the angle of the structures is quite consistent with the shape of the peak region. The fact that these structures become more prominent through this analysis suggests that these turbulent bands arise in transitional flows due to their large amplification (sensitivity to disturbances).

3.2. *Plane Poiseuille flow at* $Re = 690$

In this subsection, we apply the proposed structured input–output analysis to investigate highly amplified flow structures in plane Poiseuille flow at $Re = 690$. Figure 5(*a–c*) compares $\|\mathcal{H}_\nabla\|_\mu$, $\|\mathcal{H}\|_\infty$ and $\|\mathcal{H}_\nabla\|_\infty$ for this flow configuration. In each panel, we also indicate the streamwise vortices with $k_x \approx 0$ and $k_z = 2$ (blue star), oblique waves with $k_x = k_z = 1$ (black circle) and TS waves with $k_x = 1$ and $k_z \approx 0$ (magenta square) that were identified as transition-inducing perturbations in Reddy *et al.* (1998). Similar to the results for plane Couette flow in figure 4, the quantities $\|\mathcal{H}\|_\infty$ and $\|\mathcal{H}_\nabla\|_\infty$ show qualitatively similar behaviour; the highest values for both correspond to streamwise streaks and vortices. In figures 5(*b*) and 5(*c*), the TS wave structure appears as a local peak

https://doi.org/10.1017/jfm.2021.762 Published online by Cambridge University Press

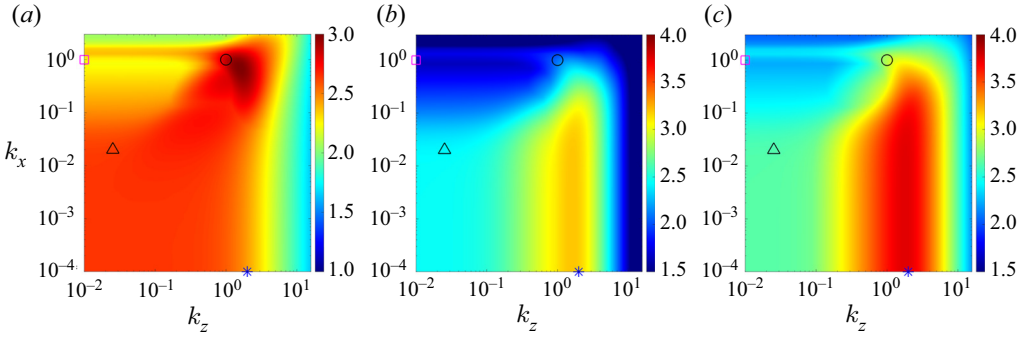


Figure 5. Contour plots of (*a*) $\log_{10}[\|\mathcal{H}_\nabla\|_\mu(k_x, k_z)]$, (*b*) $\log_{10}[\|\mathcal{H}\|_\infty(k_x, k_z)]$ and (*c*) $\log_{10}[\|\mathcal{H}_\nabla\|_\infty(k_x, k_z)]$ for plane Poiseuille flow at $Re = 690$. Here the blue star, $k_x \approx 0$, $k_z = 2$, marks streamwise vortices; the black circle, $k_x = k_z = 1$, marks oblique waves; the magenta square, $k_x = 1$, $k_z \approx 0$, marks TS waves studied by Reddy *et al.* (1998). The black triangle, $\lambda_x = 314$, $\lambda_z = 248$, indicates the wavelengths of the oblique turbulent band at $Re = 690$ observed in Kanazawa (2018).

with a magnitude that is about an order of magnitude smaller than the values associated with the streamwise vortices in $\|\mathcal{H}_\nabla\|_\infty$ and $\|\mathcal{H}\|_\infty$. In these two panels, the values for the oblique waves are of a similar order of magnitude to that of the peak corresponding to the TS waves in $\|\mathcal{H}\|_\infty$ and slightly higher in $\|\mathcal{H}_\nabla\|_\infty$. These findings agree with previous analyses of $\|\mathcal{H}\|_\infty$ in Jovanović (2004) and Schmid (2007). The similarity of the $\|\mathcal{H}_\nabla\|_\infty$ and $\|\mathcal{H}\|_\infty$ results indicates that an unstructured feedback interconnection does not lead to substantial changes in the most prominent structures.

The overall shape of $\|\mathcal{H}_\nabla\|_\mu$ is somewhat different from that of either $\|\mathcal{H}\|_\infty$ or $\|\mathcal{H}_\nabla\|_\infty$. The streamwise elongated structures that are dominant in figure 5(*b*,*c*) have a lesser but still large magnitude, while the peak value corresponds to oblique waves. The TS wave corresponds to a local peak in $\|\mathcal{H}_\nabla\|_\mu$, but the magnitudes are smaller than the peak values associated with oblique waves. This result is consistent with findings of Reddy *et al.* (1998, figure 19) showing that oblique waves require slightly less perturbation energy to trigger turbulence in plane Poiseuille flow than streamwise vortices. Both the peak region and the large region of very high values in the bottom left quadrant of figure 5(*a*) are consistent with the short-time-scale NLOP of plane Poiseuille flow, which was shown to be spatially localized with streamwise wavelength larger than spanwise wavelength (Farano *et al.* 2015). These results indicate that the inclusion of structured uncertainty uncovers a broader range of transition-inducing structures and correctly orders their relative amplification in the sense of their transition-inducing potential.

There is evidence that the oblique turbulent bands that are observed in very-large-channel studies also play a role in transition. Their ability to trigger transition has been exploited in a number of studies that employ flow fields with sustained oblique turbulent bands at a relatively high *Re* as the initial conditions to trigger the banded turbulent–laminar patterns associated with transitioning flows at a Reynolds number of interest (e.g. Tsukahara *et al.* 2005; Tuckerman *et al.* 2014; Tao *et al.* 2018; Xiao & Song 2020). The characteristic wavelength pair ($\lambda_x = 314$, $\lambda_z = 248$) associated with this structure in plane Poiseuille flow at $Re = 690$ (estimated from Kanazawa (2018, figure 5.1*b*)) is indicated in each panel of figure 5 using a black triangle. These characteristic wavelengths are located within the range of large values of $\|\mathcal{H}_\nabla\|_\mu$. They are not associated with peak regions of $\|\mathcal{H}\|_\infty$ or $\|\mathcal{H}_\nabla\|_\infty$ in figures 5(*b*) or 5(*c*), although a footprint of these flow structures is visible in both. Figure 5(*a*) indicates that the flow

https://doi.org/10.1017/jfm.2021.762 Published online by Cambridge University Press

structure associated with the oblique turbulent band has a similar amplification under structured forcing to that of streamwise elongated structures, although both of their magnitudes are smaller than that associated with the oblique waves. Further analysis of these structures and their role in transition is a topic of ongoing work.

3.3. *Componentwise structure of nonlinearity: weakening of the lift-up mechanism*

The results in the previous subsections, particularly the differences between $\|\mathcal{H}_\nabla\|_\mu$ and $\|\mathcal{H}_\nabla\|_\infty$ in figures 4 and 5, highlight the role of the feedback interconnection structure in the identification of the perturbations to which the flow is most sensitive. In particular, the imposition of the componentwise structure leads to lesser prominence of streamwise elongated structures ($k_x \approx 0$, $k_z = 2$) in $\|\mathcal{H}_\nabla\|_\mu$ compared with $\|\mathcal{H}\|_\infty$ or $\|\mathcal{H}_\nabla\|_\infty$ in both plane Couette flow and Poiseuille flow (see figures 4 and 5).

The mechanisms underlying the differences in $\|\mathcal{H}_\nabla\|_\mu$ and $\|\mathcal{H}_\nabla\|_\infty$ can be analysed by isolating the effect of forcing in each component of the momentum equation, i.e. f_x, f_y, f_z in (2.2), on the amplification of each velocity component u, v, w. These nine quantities are associated with $\|\mathcal{H}_{ij}\|_\infty$, where the spatio-temporal frequency response operator $\mathcal{H}_{ij}$ from each forcing component ($j = x, y, z$) to each velocity component ($i = u, v, w$) is given by (Jovanović & Bamieh 2005)

$$\mathcal{H}_{ij} = \hat{\mathcal{C}}_i(\mathrm{i}\omega\mathcal{I}_{2\times 2} - \hat{\mathcal{A}})^{-1}\hat{\mathcal{B}}_j \tag{3.3}$$

with

$$\hat{\mathcal{B}}_x := \hat{\mathcal{B}}\,[\mathcal{I} \quad 0 \quad 0]^{\mathrm{T}}, \quad \hat{\mathcal{B}}_y := \hat{\mathcal{B}}\,[0 \quad \mathcal{I} \quad 0]^{\mathrm{T}}, \quad \hat{\mathcal{B}}_z := \hat{\mathcal{B}}\,[0 \quad 0 \quad \mathcal{I}]^{\mathrm{T}}, \tag{3.4a}$$

$$\hat{\mathcal{C}}_u := [\mathcal{I} \quad 0 \quad 0]\,\hat{\mathcal{C}}, \quad \hat{\mathcal{C}}_v := [0 \quad \mathcal{I} \quad 0]\,\hat{\mathcal{C}}, \quad \hat{\mathcal{C}}_w := [0 \quad 0 \quad \mathcal{I}]\,\hat{\mathcal{C}}. \tag{3.4b}$$

These quantities were analysed in Jovanović (2004) and Schmid (2007). Those results indicate that the most significant amplification is seen when forcing is applied in the cross-stream and the output is the streamwise velocity component, i.e. that associated with respective frequency response operators $\mathcal{H}_{uy}$, $\mathcal{H}_{uz}$ and input–output pathway $f_y \to u$, $f_z \to u$. Similar behaviour occurs if we isolate $\mathcal{H}_\nabla$ by examining each input–output response pathway:

$$\mathcal{H}_{\nabla ij} := \hat{\nabla}\mathcal{H}_{ij}. \tag{3.5}$$

In that prior work, the input forcing (applied either directly to the LNS (top block in figure 1) or through a feedback interconnection) was unstructured in the sense that there was no restriction in terms of the permissible input–output pathways. The behaviour of the largest $\|\mathcal{H}_{ij}\|_\infty$ ($\|\mathcal{H}_{\nabla ij}\|_\infty$) response therefore dominates the overall $\|\mathcal{H}\|_\infty$ ($\|\mathcal{H}_\nabla\|_\infty$) response.

The structured input–output analysis framework introduced here instead imposes a correlation between each component of the modelled forcing $f_{x,\xi}$, $f_{y,\xi}$ and $f_{z,\xi}$ and the respective velocity components u, v and w by constraining the feedback interconnection to retain the componentwise structure of our input–output model of the forcing. This model of the forcing in terms of componentwise input–output relationships from $\boldsymbol{\nabla} u$, $\boldsymbol{\nabla} v$ and $\boldsymbol{\nabla} w$ to the respective components $f_{x,\xi} = -\boldsymbol{u}_\xi \cdot \boldsymbol{\nabla} u$, $f_{y,\xi} = -\boldsymbol{u}_\xi \cdot \boldsymbol{\nabla} v$ and $f_{z,\xi} = -\boldsymbol{u}_\xi \cdot \boldsymbol{\nabla} w$ with the gain defined in terms of $-\boldsymbol{u}_\xi$ constrains the feedback relationships such that each component of the forcing is most strongly influenced by that component of the velocity field and velocity gradient. These constraints on the permissible feedback pathways within our model of the nonlinear interactions limit the influence of the input–output pathways

https://doi.org/10.1017/jfm.2021.762 Published online by Cambridge University Press

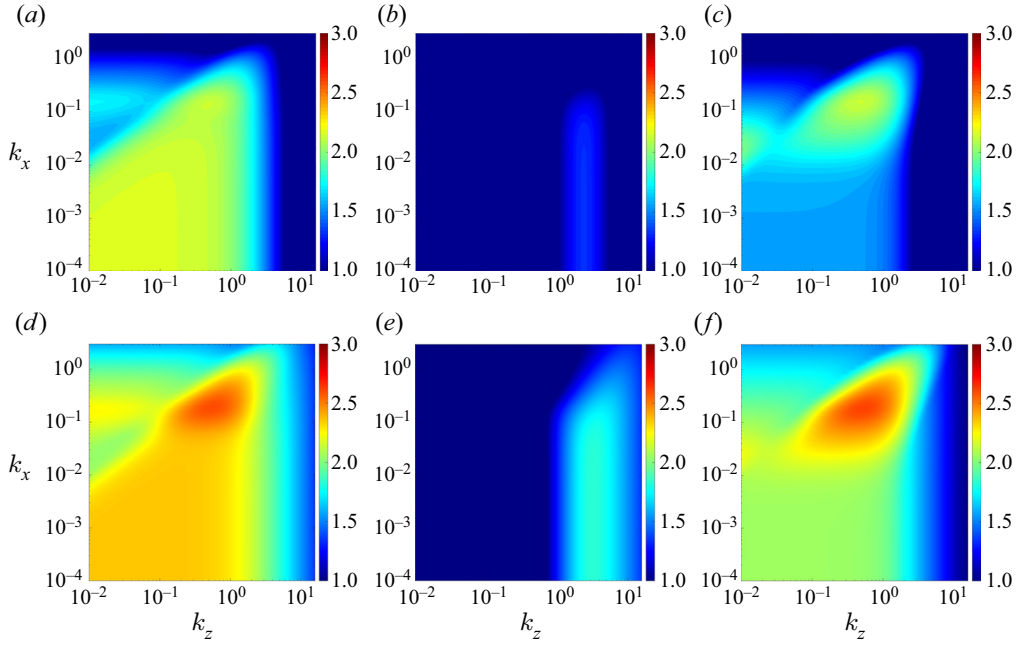


Figure 6. Contour plots of (*a*) $\log_{10}[\|\mathcal{H}_{ux}\|_\infty(k_x, k_z)]$, (*b*) $\log_{10}[\|\mathcal{H}_{vy}\|_\infty(k_x, k_z)]$, (*c*) $\log_{10}[\|\mathcal{H}_{wz}\|_\infty(k_x, k_z)]$, (*d*) $\log_{10}[\|\mathcal{H}_{\nabla ux}\|_\infty(k_x, k_z)]$, (*e*) $\log_{10}[\|\mathcal{H}_{\nabla vy}\|_\infty(k_x, k_z)]$ and (*f*) $\log_{10}[\|\mathcal{H}_{\nabla wz}\|_\infty(k_x, k_z)]$ for plane Couette flow at $Re = 358$.

$f_y \to u$ and $f_z \to u$. The structured input–output response $\|\mathcal{H}_\nabla\|_\mu$ is instead associated with input–output pathways $f_x \to u$, $f_y \to v$ and $f_z \to w$ as illustrated in figures 6 and 7, which plot $\|\mathcal{H}_{ux}\|_\infty$, $\|\mathcal{H}_{vy}\|_\infty$, $\|\mathcal{H}_{wz}\|_\infty$, $\|\mathcal{H}_{\nabla ux}\|_\infty$, $\|\mathcal{H}_{\nabla vy}\|_\infty$ and $\|\mathcal{H}_{\nabla wz}\|_\infty$ for the plane Couette and Poiseuille cases respectively discussed in §§ 3.1 and 3.2. Here, we can see that the results of structured input–output analysis $\|\mathcal{H}_\nabla\|_\mu$ for both of these flows in figures 4(*a*) and 5(*a*) resemble the combined effect of this limited set of input–output pathways. Moreover, the quantity $\|\mathcal{H}_\nabla\|_\mu$ at each wavenumber pair (k_x, k_z) is lower bounded by $\|\mathcal{H}_{\nabla ux}\|_\infty$, $\|\mathcal{H}_{\nabla vy}\|_\infty$ and $\|\mathcal{H}_{\nabla wz}\|_\infty$ as described in theorem 3.1, whose proof is provided in Appendix A.1. The relationship in theorem 3.1 is evident when comparing results in figures 4(*a*) and 6(*d–f*) for plane Couette flow and comparing results in figures 5(*a*) and 7(*d–f*) for plane Poiseuille flow.

THEOREM 3.1. *Given wavenumber pair* (k_x, k_z),

$$\|\mathcal{H}_\nabla\|_\mu \geqslant max[\|\mathcal{H}_{\nabla ux}\|_\infty, \|\mathcal{H}_{\nabla vy}\|_\infty, \|\mathcal{H}_{\nabla wz}\|_\infty]. \tag{3.6}$$

The input–output pathways that dominate the overall unstructured response $\|\mathcal{H}\|_\infty$ ($\|\mathcal{H}_{uy}\|_\infty$ and $\|\mathcal{H}_{uz}\|_\infty$) emphasize amplification of streamwise streaks by cross-stream forcing, i.e. the lift-up mechanism (see e.g. the discussion in Jovanović (2021) for further details). The lift-up mechanism therefore appears to be weakened through the imposition of the componentwise structure of the nonlinearity, which is consistent with results suggesting that nonlinear mechanisms disadvantage the growth of streaks (e.g. Duguet *et al.* 2013; Brandt 2014). These results suggest that the preservation of the componentwise structure of nonlinearity within the proposed approach enables the method to capture important nonlinear effects, leading to better agreement with DNS and experimental

https://doi.org/10.1017/jfm.2021.762 Published online by Cambridge University Press

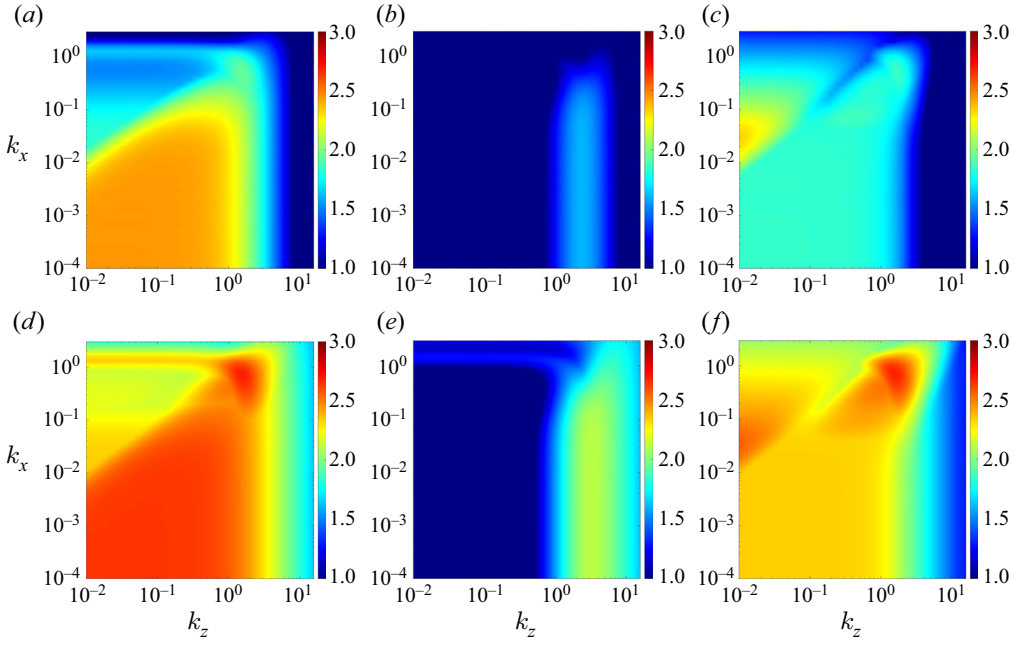


Figure 7. Contour plots of (*a*) $\log_{10}[\|\mathcal{H}_{ux}\|_\infty(k_x, k_z)]$, (*b*) $\log_{10}[\|\mathcal{H}_{vy}\|_\infty(k_x, k_z)]$, (*c*) $\log_{10}[\|\mathcal{H}_{wz}\|_\infty(k_x, k_z)]$, (*d*) $\log_{10}[\|\mathcal{H}_{\nabla ux}\|_\infty(k_x, k_z)]$, (*e*) $\log_{10}[\|\mathcal{H}_{\nabla vy}\|_\infty(k_x, k_z)]$ and (*f*) $\log_{10}[\|\mathcal{H}_{\nabla wz}\|_\infty(k_x, k_z)]$ for plane Poiseuille flow at $Re = 690$.

studies and nonlinear analysis of the perturbations that require less energy to initiate transition, e.g. NLOP.

4. Reynolds number dependence

In this section, we aggregate results across a range of (k_x, k_z) scales to study the Reynolds number dependence and the associated scaling law of $\|\mathcal{H}_\nabla\|_\mu$ for both plane Couette flow and plane Poiseuille flow. In particular, we compute

$$\|\mathcal{H}_\nabla\|_\mu^M := \max_{k_z,\, k_x} \|\mathcal{H}_\nabla\|_\mu(k_x, k_z), \tag{4.1}$$

where $\max_{k_z,\, k_x}$ corresponds to the maximum value over the wavenumber pairs (k_x, k_z) in the computational range of $k_x \in [10^{-4}, 10^{0.48}]$ and $k_z \in [10^{-2}, 10^{1.2}]$.

In order to compare our results with the scaling relationships of $\|\mathcal{H}\|_\infty$ previously described in the literature and to isolate the effect of the structure in the feedback loop, we analogously define

$$\|\mathcal{H}\|_\infty^M := \max_{k_z,\, k_x} \|\mathcal{H}\|_\infty(k_x, k_z), \tag{4.2a}$$

$$\|\mathcal{H}_\nabla\|_\infty^M := \max_{k_z,\, k_x} \|\mathcal{H}_\nabla\|_\infty(k_x, k_z). \tag{4.2b}$$

The scaling of quantities related to $\|\mathcal{H}\|_\infty$ and $\|\mathcal{H}\|_\infty^M$ with different input–output pathways, i.e. different $\hat{\mathcal{B}}$ and $\hat{\mathcal{C}}$ matrices in (3.4), has been widely studied. For example, Trefethen *et al.* (1993, table 1) showed that $\sup_{\omega\in\mathbb{R}}\|(\mathrm{i}\omega\mathcal{I} - \hat{\mathcal{A}})^{-1}\| \sim Re^2$ for plane

https://doi.org/10.1017/jfm.2021.762 Published online by Cambridge University Press

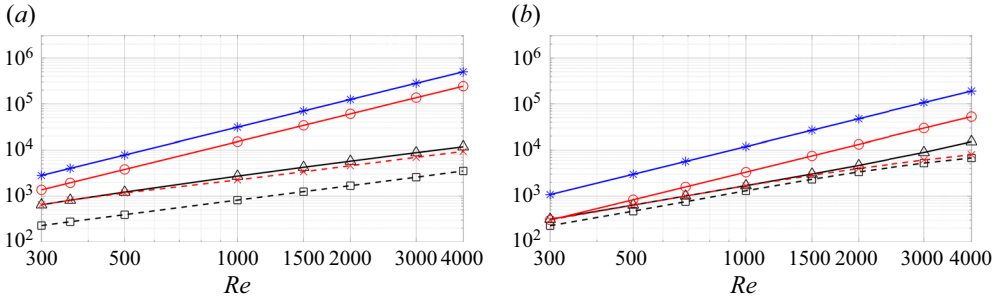


Figure 8. The Reynolds number dependence of $\|\mathcal{H}_\nabla\|_\mu^M$ (black triangle); $\|\mathcal{H}\|_\infty^M$ (red circle); $\|\mathcal{H}_\nabla\|_\infty^M$ (blue star); $\|\mathcal{H}_\nabla\|_\mu(1, 1)$ (black square). (*a*) Plane Couette flow with red crosses marking $\|\mathcal{H}_\nabla\|_\mu(0.19, 0.58)$ and (*b*) plane Poiseuille flow with red crosses marking $\|\mathcal{H}_\nabla\|_\mu(0.69, 1.56)$.

Couette flow and plane Poiseuille flow are respectively associated with wavenumber pairs $(k_x, k_z) = (0, 1.18)$ and $(k_x, k_z) = (0, 1.62)$. Here, the operator norm $\|\cdot\|$ is defined such that $\sup_{\omega\in\mathbb{R}}\|\cdot\|$ is equivalent to the definition of $\|\cdot\|_\infty$ employed in (3.1). Kreiss *et al.* (1994) showed that the related quantity maximized over a range of (k_x, k_z), i.e.

$$\max_{\mathbb{R}e[s]\geqslant 0}\|(s\mathcal{I} - \hat{\mathcal{A}})^{-1}\| \sim Re^2 \tag{4.3}$$

for plane Couette flow, where $\mathbb{R}e[s]$ denotes the real part of the Laplace variable s. Jovanović (2004, theorem 11) analytically derived the same $\sim Re^2$ scaling for the special case of $\|\mathcal{H}\|_\infty$ restricted to $k_x = 0$ for both plane Couette and Poiseuille flows.

Figure 8 plots the quantities in (4.1)–(4.2) as a function of Reynolds number ($Re \in [300, 4000]$) for plane Couette flow and plane Poiseuille flow. The upper bound of $Re = 4000$ was selected to remain below the known linear stability limit for plane Poiseuille flow of $Re \simeq 5772$ (Orszag 1971). As expected, all of these quantities increase with Reynolds number and the values of $\|\mathcal{H}_\nabla\|_\infty^M$ are larger than those of $\|\mathcal{H}_\nabla\|_\mu^M$. We obtain a Reynolds number scaling of each quantity by fitting the lines in figure 8 to $c_0 Re^\eta$, where c_0 is a constant scalar and η is the corresponding scaling exponent. The results show that $\|\mathcal{H}\|_\infty^M$ and $\|\mathcal{H}_\nabla\|_\infty^M$ scale as $\sim Re^2$ in the range $Re \in [300, 4000]$ for both plane Couette and plane Poiseuille flows. This scaling is consistent with the results in Trefethen *et al.* (1993) for the frequency response operator with identity operators for $\hat{\mathcal{C}}$ and $\hat{\mathcal{B}}$ as well as the related quantity in Kreiss *et al.* (1994). The fact that the scaling of this quantity for the modified frequency response operator $\mathcal{H}_\nabla$ is the same as that of $\mathcal{H}$ suggests that adding an unstructured uncertainty in the feedback loop to represent the nonlinear interactions does not change the Reynolds number scaling.

The quantity $\|\mathcal{H}_\nabla\|_\mu^M$ in figure 8 instead shows scalings of $\sim Re^{1.1}$ over $Re \in [300, 4000]$ for plane Couette flow and $\sim Re^{1.5}$ for plane Poiseuille flow in the range $Re \in [500, 4000]$. The difference between the scaling of $\|\mathcal{H}_\nabla\|_\mu^M$ and the $\sim Re^2$ scaling associated with either $\|\mathcal{H}\|_\infty^M$ or $\|\mathcal{H}_\nabla\|_\infty^M$ again arises through the imposition of the componentwise structure of nonlinearity. As discussed in § 3.3, the reduced scaling is related to the smaller amplification in the input–output pathways $f_x \to u, f_y \to v$ and $f_z \to w$ and associated $f_x \to \nabla u$, $f_y \to \nabla v$ and $f_z \to \nabla w$. The scaling for these input–output pathways can be evaluated directly through

$$\|\mathcal{H}_{\nabla ij}\|_\infty^M := \max_{k_z, k_x}\|\mathcal{H}_{\nabla ij}\|_\infty(k_x, k_z). \tag{4.4}$$

https://doi.org/10.1017/jfm.2021.762 Published online by Cambridge University Press

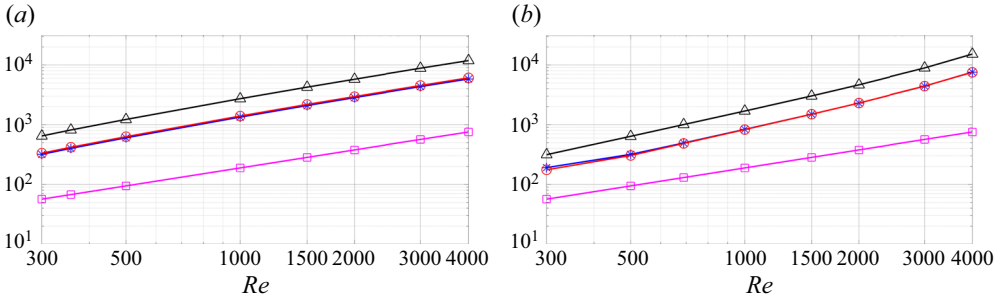


Figure 9. The Reynolds number dependence of $\|\mathcal{H}_\nabla\|_\mu^M$ (black triangle); $\|\mathcal{H}_{\nabla ux}\|_\infty^M$ (blue star); $\|\mathcal{H}_{\nabla vy}\|_\infty^M$ (magenta square); $\|\mathcal{H}_{\nabla wz}\|_\infty^M$ (red circle). (*a*) Plane Couette flow and (*b*) plane Poiseuille flow.

These quantities are plotted in figure 9 alongside $\|\mathcal{H}_\nabla\|_\mu^M$. Performing a similar fit we find that both $\|\mathcal{H}_{\nabla ux}\|_\infty^M$ and $\|\mathcal{H}_{\nabla wz}\|_\infty^M$ scale as $\sim Re^{1.1}$ for plane Couette flow and $\sim Re^{1.5}$ for plane Poiseuille flow, which matches the scaling of $\|\mathcal{H}_\nabla\|_\mu^M$. On the other hand, $\|\mathcal{H}_{\nabla vy}\|_\infty^M$ is much smaller than these three quantities and scales as $\|\mathcal{H}_{\nabla vy}\|_\infty^M \sim Re$ for both plane Couette and Poiseuille flows.

In order to understand the role of the oblique waves in this scaling, we also plot the quantity $\|\mathcal{H}_\nabla\|_\mu(1, 1)$ corresponding to the wavenumber pair associated with the oblique waves discussed in §§ 3.1 and 3.2 in figure 8. In both flows, these values are lower than and not exactly parallel with $\|\mathcal{H}_\nabla\|_\mu^M$, indicating that they are not associated with the peak amplification of $\|\mathcal{H}_\nabla\|_\mu$ in figures 4(*a*) and 5(*a*). However, they do seem to provide the majority of the contribution to $\|\mathcal{H}_\nabla\|_\mu^M$. This observation is consistent with figures 4(*a*) and 5(*a*), where $(k_x, k_z) = (1, 1)$ is close to but different from the (k_x^M, k_z^M) wavenumber pair that reaches the maximum value of $\|\mathcal{H}_\nabla\|_\mu(k_x, k_z)$ defined as

$$(k_x^M, k_z^M) := \arg\max_{k_x, k_z} \|\mathcal{H}_\nabla\|_\mu(k_x, k_z). \tag{4.5}$$

These wavenumber pairs are $(k_x^M, k_z^M) = (0.19, 0.58)$ for plane Couette flow at $Re = 358$ and $(k_x^M, k_z^M) = (0.69, 1.56)$ for plane Poiseuille flow at $Re = 690$. We also plot the Reynolds number dependence of $\|\mathcal{H}_\nabla\|_\mu(0.19, 0.58) \sim Re$ for plane Couette flow and $\|\mathcal{H}_\nabla\|_\mu(0.69, 1.56) \sim Re^{1.3}$ for plane Poiseuille flow as red cross markers in figure 8. Here, we observe that they overlap with $\|\mathcal{H}_\nabla\|_\mu^M$ at low Reynolds numbers, but deviate as the Reynolds number increases leading to a reduced Re scaling compared with $\|\mathcal{H}_\nabla\|_\mu^M$. These results show that these oblique flow structures continue to show very high (close to the maximum overall amplification value) throughout the Reynolds number range. However, the wavenumber pair (k_x^M, k_z^M) that reaches the maximum value over $\|\mathcal{H}_\nabla\|_\mu(k_x, k_z)$ depends on the Reynolds number.

The observed importance and analytical tractability of streamwise elongated structures have motivated previous analysis of the streamwise constant ($k_x = 0$) component of the frequency response operator. In order to compare our analysis with these results, we also evaluate this behaviour by computing analogous quantities

$$\|\mathcal{H}_\nabla\|_\mu^{sc} := \max_{k_z,\, k_x = 10^{-4}} \|\mathcal{H}_\nabla\|_\mu(k_x, k_z), \tag{4.6a}$$

$$\|\mathcal{H}_{\nabla ij}\|_\infty^{sc} := \max_{k_z,\, k_x = 10^{-4}} \|\mathcal{H}_{\nabla ij}\|_\infty(k_x, k_z), \tag{4.6b}$$

https://doi.org/10.1017/jfm.2021.762 Published online by Cambridge University Press

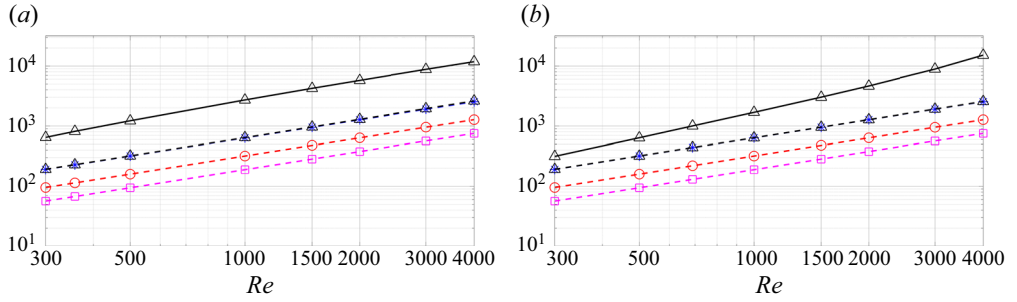


Figure 10. The Reynolds number dependence of $\|\mathcal{H}_\nabla\|_\mu^M$ (black triangle, solid line); $\|\mathcal{H}_\nabla\|_\mu^{sc}$ (balck triangle, dashed line); $\|\mathcal{H}_{\nabla ux}\|_\infty^{sc}$ (blue star); $\|\mathcal{H}_{\nabla vy}\|_\infty^{sc}$ (magenta square); $\|\mathcal{H}_{\nabla wz}\|_\infty^{sc}$ (red circle). (*a*) Plane Couette flow and (*b*) plane Poiseuille flow.

which restricts the streamwise wavenumber to $k_x = 10^{-4}$ to approximate the streamwise constant modes. In figure 10, we replot $\|\mathcal{H}_\nabla\|_\mu^M$ alongside $\|\mathcal{H}_\nabla\|_\mu^{sc}$ (black triangle, dashed line), and observe that $\|\mathcal{H}_\nabla\|_\mu^{sc} \sim Re$ for both plane Couette and Poiseuille flows. Figure 10 also shows $\|\mathcal{H}_{\nabla ux}\|_\infty^{sc}$, $\|\mathcal{H}_{\nabla vy}\|_\infty^{sc}$ and $\|\mathcal{H}_{\nabla wz}\|_\infty^{sc}$. Here, we find that $\|\mathcal{H}_\nabla\|_\mu^{sc}$ overlaps with $\|\mathcal{H}_{\nabla ux}\|_\infty^{sc}$ and thus shows the same scaling $\sim Re$. These three input–output pathways $\|\mathcal{H}_{\nabla ij}\|_\infty^{sc}$ ($ij = ux, vy, wz$) scale as $\sim Re$ for both plane Couette and Poiseuille flows. This behaviour is consistent with the results in Jovanović (2004, theorem 11), which showed that $\|\mathcal{H}_{ij}\|_\infty \sim Re$ ($ij = ux, vy, wz$) when it is restricted to $k_x = 0$ for both plane Couette and plane Poiseuille flows. The following theorem provides an analogous analytical Re scaling for $\|\mathcal{H}_{\nabla ij}\|_\infty$ at $k_x = 0$, i.e. the streamwise constant component.

THEOREM 4.1. *Given streamwise constant ($k_x = 0$) plane Couette flow or plane Poiseuille flow, each component of $\|\mathcal{H}_{\nabla ij}\|_\infty$ ($i = u, v, w$ and $j = x, y, z$) scales as*

$$\begin{bmatrix} \|\mathcal{H}_{\nabla ux}\|_\infty & \|\mathcal{H}_{\nabla uy}\|_\infty & \|\mathcal{H}_{\nabla uz}\|_\infty \\ \|\mathcal{H}_{\nabla vx}\|_\infty & \|\mathcal{H}_{\nabla vy}\|_\infty & \|\mathcal{H}_{\nabla vz}\|_\infty \\ \|\mathcal{H}_{\nabla wx}\|_\infty & \|\mathcal{H}_{\nabla wy}\|_\infty & \|\mathcal{H}_{\nabla wz}\|_\infty \end{bmatrix} = \begin{bmatrix} Re\, h_{\nabla ux}(k_z) & Re^2\, h_{\nabla uy}(k_z) & Re^2\, h_{\nabla uz}(k_z) \\ 0 & Re\, h_{\nabla vy}(k_z) & Re\, h_{\nabla vz}(k_z) \\ 0 & Re\, h_{\nabla wy}(k_z) & Re\, h_{\nabla wz}(k_z) \end{bmatrix}, \tag{4.7}$$

where functions $h_{\nabla ij}(k_z)$ are independent of Re.

The proof of theorem 4.1 in Appendix A.2 follows the procedure in Jovanović (2004), Jovanović & Bamieh (2005) and Jovanović (2021), which involves the change of variable $\Omega := \omega Re$. Comparing scaling of this $\|\mathcal{H}_{\nabla ij}\|_\infty$ in theorem 4.1 with that of $\|\mathcal{H}_{ij}\|_\infty$ at $k_x = 0$ in Jovanović (2004, theorem 11) shows that the modification of the operator to provide the output $\hat{\nabla}\hat{u}$, $\hat{\nabla}\hat{v}$ and $\hat{\nabla}\hat{w}$ does not modify the Reynolds number scaling, which is expected since this operation amounts to a Reynolds-number-independent transformation of the system output.

Combining results in theorems 3.1 and 4.1, we have the following corollary 4.2 providing an analytical lower bound on $\|\mathcal{H}_\nabla\|_\mu$ at $k_x = 0$.

COROLLARY 4.2. *Given streamwise constant ($k_x = 0$) plane Couette flow or plane Poiseuille flow,*

$$\|\mathcal{H}_\nabla\|_\mu(0, k_z) \geqslant max[Re\, h_{\nabla ux}(k_z), Re\, h_{\nabla vy}(k_z), Re\, h_{\nabla wz}(k_z)], \tag{4.8}$$

where functions $h_{\nabla ij}(k_z)$ with $ij = ux, vy, wz$ are independent of Re.

https://doi.org/10.1017/jfm.2021.762 Published online by Cambridge University Press

The previous numerical observations of $\|\mathcal{H}_\nabla\|_\mu^{sc} \sim Re$ in figure 10 for both plane Couette and plane Poiseuille flows are consistent with corollary 4.2. The reduced scaling exponent η of the largest structured gain $\|\mathcal{H}_\nabla\|_\mu^{M} \sim Re^\eta$ observed here compared with $\eta = 2$ for unstructured gain (Trefethen *et al.* 1993; Kreiss *et al.* 1994; Jovanović 2004) further highlights the importance of the componentwise structure of nonlinearity imposed in this framework, this structure is what appears to weaken the large amplification associated with the lift-up mechanism.

5. Conclusions and future work

This work proposes a structured input–output analysis that augments traditional analysis of the spatio-temporal frequency response of the LNS with structured uncertainty. The structure preserves the componentwise input–output structure of the nonlinearity in the NS equations. We then analyse the spatio-temporal response of the resulting feedback interconnection between the LNS equations and the structured forcing in terms of the structured singular value of the associated spatio-temporal frequency response operator.

We apply structured input–output analysis to transitional plane Couette and plane Poiseuille flows. Comparisons of the results with those of traditional analysis and an unstructured feedback interconnection indicate that the addition of a structured feedback interconnection enables a wider range of known dominant flow structures to be identified without the computational burden of nonlinear optimization or extensive simulations. More specifically, the results for transitional plane Couette flow reproduce the findings from DNS (Reddy *et al.* 1998) and NLOP analysis (Rabin *et al.* 2012) in showing that oblique waves require less energy to induce transition than the streamwise elongated structures emphasized in traditional input–output analysis. In plane Poiseuille flow the results again predict the oblique wave structure as in DNS (Reddy *et al.* 1998). They also highlight the importance of spatially localized structures with a streamwise wavelength larger than spanwise similar to the NLOP (Farano *et al.* 2015). The framework also reproduces the oblique turbulent bands (Prigent *et al.* 2003; Kanazawa 2018) that have been associated with transitioning flows with very large channel sizes ($\sim O(100)$ times the channel half-height) in both experiments and DNS.

The agreement between the predictions from structured input–output analysis and observation in experiments, DNS and NLOP computations indicates that the structured feedback interconnection reproduces important nonlinear effects. Our analysis suggests that restricting the feedback pathways preserves the structure of the nonlinear mechanisms that weaken the streaks developed through the lift-up effect, in which cross-stream forcing amplifies streamwise streaks (Ellingsen & Palm 1975; Landahl 1975; Brandt 2014). The Reynolds number dependence observed in our studies further supports the notion that imposing a structured feedback interconnection based on certain input–output properties associated with the nonlinearity in the NS equations leads to a weakening of the amplification of streamwise elongated structures.

The results here suggest the promise of this computationally tractable approach and open up many directions for future work. Further refinement of the structured uncertainty may provide additional physical insight. This extension and the development of the associated computational tools are the subjects of ongoing work. The results here are associated with the maximum amplification over all frequencies but it may be also interesting to isolate each temporal frequency and examine the frequency that maximizes the amplification under this structured feedback interconnection. Another natural direction is an extension to pipe flow, where subcritical transition is also widely studied (e.g. Hof, Juel & Mullin 2003; Peixinho & Mullin 2007; Eckhardt *et al.* 2007; Mellibovsky & Meseguer

https://doi.org/10.1017/jfm.2021.762 Published online by Cambridge University Press

2009; Mullin 2011; Pringle & Kerswell 2010; Pringle, Willis & Kerswell 2012; Barkley 2016). Adaptations of this approach to the fully developed turbulent regime, where the resolvent framework and input–output analysis have provided important insights, are another direction of ongoing study.

Funding. The authors gratefully acknowledge support from the US National Science Foundation (NSF) through grant number CBET 1652244 and the Office of Naval Research (ONR) through grant number N00014-18-1-2534. C.L. greatly appreciates the support from the Chinese Scholarship Council.

Declaration of interests. The authors report no conflict of interest.

Author ORCIDs.
Chang Liu https://orcid.org/0000-0003-2091-6545;
Dennice F. Gayme https://orcid.org/0000-0003-0330-415X.

Appendix A. Proof of theorems 3.1 and 4.1

A.1. *Proof of theorem* 3.1

Proof. We define the following sets of uncertainty:

$$\hat{\boldsymbol{U}}_{\Xi,ux} := \left\{ \mathrm{diag}\left(-\hat{\boldsymbol{u}}_\xi^{\mathrm{T}}, \boldsymbol{0}, \boldsymbol{0}\right) : -\hat{\boldsymbol{u}}_\xi^{\mathrm{T}} \in \mathbb{C}^{N_y \times 3N_y} \right\}, \tag{A1a}$$

$$\hat{\boldsymbol{U}}_{\Xi,vy} := \left\{ \mathrm{diag}\left(\boldsymbol{0}, -\hat{\boldsymbol{u}}_\xi^{\mathrm{T}}, \boldsymbol{0}\right) : -\hat{\boldsymbol{u}}_\xi^{\mathrm{T}} \in \mathbb{C}^{N_y \times 3N_y} \right\}, \tag{A1b}$$

$$\hat{\boldsymbol{U}}_{\Xi,wz} := \left\{ \mathrm{diag}\left(\boldsymbol{0}, \boldsymbol{0}, -\hat{\boldsymbol{u}}_\xi^{\mathrm{T}}\right) : -\hat{\boldsymbol{u}}_\xi^{\mathrm{T}} \in \mathbb{C}^{N_y \times 3N_y} \right\}. \tag{A1c}$$

Here, $\boldsymbol{0} \in \mathbb{C}^{N_y \times 3N_y}$ is a zero matrix with size $N_y \times 3N_y$. Then, using the definition of the structured singular value in definition 2.1, we have

$$\begin{aligned}
&\mu_{\hat{\boldsymbol{U}}_{\Xi,ux}}\left[\boldsymbol{H}_\nabla(k_x, k_z, \omega)\right] \\
&\quad = \frac{1}{\min\{\bar{\sigma}[\hat{\boldsymbol{u}}_{\Xi,ux}] \,:\, \hat{\boldsymbol{u}}_{\Xi,ux} \in \hat{\boldsymbol{U}}_{\Xi,ux},\ \det[\boldsymbol{I} - \boldsymbol{H}_\nabla(k_x, k_z, \omega)\hat{\boldsymbol{u}}_{\Xi,ux}] = 0\}} && \text{(A2a)} \\
&\quad = \frac{1}{\min\{\bar{\sigma}[-\hat{\boldsymbol{u}}_\xi^{\mathrm{T}}] \,:\, -\hat{\boldsymbol{u}}_\xi^{\mathrm{T}} \in \mathbb{C}^{N_y \times 3N_y},\ \det[\boldsymbol{I}_{3N_y} - \boldsymbol{H}_{\nabla ux}(k_x, k_z, \omega)(-\hat{\boldsymbol{u}}_\xi^{\mathrm{T}})] = 0\}} && \text{(A2b)} \\
&\quad = \bar{\sigma}[\boldsymbol{H}_{\nabla ux}(k_x, k_z, \omega)]. && \text{(A2c)}
\end{aligned}$$

Here, the equality (A2*a*) is obtained by substituting the uncertainty set in (A1*a*) into definition 2.1. The equality (A2*b*) is obtained by performing block diagonal partition of terms inside of det[·] and employing zeros in the uncertainty set in (A1*a*). Here, $\boldsymbol{H}_{\nabla ux}$ is the discretization of $\mathcal{H}_{\nabla ux}$ and $\boldsymbol{I}_{3N_y} \in \mathbb{C}^{3N_y \times 3N_y}$ in (A2*b*) with size $(3N_y \times 3N_y)$, whereas $\boldsymbol{I} \in \mathbb{C}^{9N_y \times 9N_y}$ in (A2*a*). The equality (A2*c*) uses the definition of unstructured singular value; see e.g. Zhou *et al.* (1996, equation (11.1)).

Similarly, we have

$$\mu_{\hat{\boldsymbol{U}}_{\Xi,vy}}[\boldsymbol{H}_\nabla(k_x, k_z, \omega)] = \bar{\sigma}[\boldsymbol{H}_{\nabla vy}(k_x, k_z, \omega)], \tag{A3a}$$

$$\mu_{\hat{\boldsymbol{U}}_{\Xi,wz}}[\boldsymbol{H}_\nabla(k_x, k_z, \omega)] = \bar{\sigma}[\boldsymbol{H}_{\nabla wz}(k_x, k_z, \omega)]. \tag{A3b}$$

Using the fact that $\hat{\boldsymbol{U}}_\Xi \supseteq \hat{\boldsymbol{U}}_{\Xi,ij}$ with $ij = ux, vy, wz$ and equalities in (A2)–(A3), we have

$$\mu_{\hat{\boldsymbol{U}}_\Xi}[\boldsymbol{H}_\nabla(k_x, k_z, \omega)] \geqslant \mu_{\hat{\boldsymbol{U}}_{\Xi,ij}}[\boldsymbol{H}_\nabla(k_x, k_z, \omega)] = \bar{\sigma}[\boldsymbol{H}_{\nabla ij}(k_x, k_z, \omega)]. \tag{A4}$$

https://doi.org/10.1017/jfm.2021.762 Published online by Cambridge University Press

Applying the supreme operation $\sup_{\omega\in\mathbb{R}}[\cdot]$ on (A4) and using the definitions of $\|\cdot\|_\mu$ and $\|\cdot\|_\infty$, we have

$$\|\mathcal{H}_\nabla\|_\mu \geqslant \|\mathcal{H}_{\nabla ux}\|_\infty, \quad \|\mathcal{H}_\nabla\|_\mu \geqslant \|\mathcal{H}_{\nabla vy}\|_\infty, \quad \|\mathcal{H}_\nabla\|_\mu \geqslant \|\mathcal{H}_{\nabla wz}\|_\infty. \tag{A5a–c}$$

This directly results in inequality (3.6) of theorem 3.1. ■

A.2. *Proof of theorem 4.1*

Proof. Under the streamwise constant $k_x = 0$ assumption for plane Couette flow or plane Poiseuille flow in theorem 4.1, the operators $\hat{\mathcal{A}}$, $\hat{\mathcal{B}}$ and $\hat{\mathcal{C}}$ can be simplified and decomposed as

$$\hat{\mathcal{A}}(k_x, k_z) = \begin{bmatrix} \frac{\hat{\nabla}^{-2}\hat{\nabla}^4}{Re} & 0 \\ -\mathrm{i}k_z U' & \frac{\hat{\nabla}^2}{Re} \end{bmatrix}, \tag{A6a}$$

$$\hat{\mathcal{B}}(k_x, k_z) = \begin{bmatrix} 0 & -k_z^2\hat{\nabla}^{-2} & -\mathrm{i}k_z\hat{\nabla}^{-2}\partial_y \\ \mathrm{i}k_z & 0 & 0 \end{bmatrix} =: \begin{bmatrix} 0 & \hat{\mathcal{B}}_{y,1} & \hat{\mathcal{B}}_{z,1} \\ \mathcal{B}_{x,2} & 0 & 0 \end{bmatrix}, \tag{A6b}$$

$$\hat{\mathcal{C}}(k_x, k_z) = \begin{bmatrix} 0 & -\mathrm{i}/k_z \\ \mathcal{I} & 0 \\ \mathrm{i}\partial_y/k_z & 0 \end{bmatrix} =: \begin{bmatrix} 0 & \hat{\mathcal{C}}_{u,2} \\ \hat{\mathcal{C}}_{v,1} & 0 \\ \hat{\mathcal{C}}_{w,1} & 0 \end{bmatrix}. \tag{A6c}$$

Here, we employ a matrix inverse formula for the lower triangle block matrix:

$$\begin{bmatrix} L_{11} & 0 \\ L_{21} & L_{22} \end{bmatrix}^{-1} = \begin{bmatrix} L_{11}^{-1} & 0 \\ -L_{22}^{-1}L_{21}L_{11}^{-1} & L_{22}^{-1} \end{bmatrix} \tag{A7}$$

to compute $(\mathrm{i}\omega\mathcal{I}_{2\times 2} - \hat{\mathcal{A}})^{-1}$. Then, we employ a change of variable $\Omega = \omega Re$ similar to Jovanović (2004), Jovanović & Bamieh (2005) and Jovanović (2021) to obtain $\mathcal{H}_{\nabla ij}$ with $i = u, v, w$, and $j = x, y, z$ as

$$\mathcal{H}_{\nabla ux} = \hat{\nabla}\hat{\mathcal{C}}_{u,2}Re(\mathrm{i}\Omega\mathcal{I} - \hat{\nabla}^2)^{-1}\hat{\mathcal{B}}_{x,2}, \tag{A8a}$$

$$\mathcal{H}_{\nabla uy} = \hat{\nabla}\hat{\mathcal{C}}_{u,2}Re(\mathrm{i}\Omega\mathcal{I} - \hat{\nabla}^2)^{-1}(-\mathrm{i}k_z U')Re(\mathrm{i}\Omega\mathcal{I} - \hat{\nabla}^{-2}\hat{\nabla}^4)^{-1}\hat{\mathcal{B}}_{y,1}, \tag{A8b}$$

$$\mathcal{H}_{\nabla uz} = \hat{\nabla}\hat{\mathcal{C}}_{u,2}Re(\mathrm{i}\Omega\mathcal{I} - \hat{\nabla}^2)^{-1}(-\mathrm{i}k_z U')Re(\mathrm{i}\Omega\mathcal{I} - \hat{\nabla}^{-2}\hat{\nabla}^4)^{-1}\hat{\mathcal{B}}_{z,1}, \tag{A8c}$$

$$\mathcal{H}_{\nabla vx} = 0, \tag{A8d}$$

$$\mathcal{H}_{\nabla vy} = \hat{\nabla}\hat{\mathcal{C}}_{v,1}Re(\mathrm{i}\Omega\mathcal{I} - \hat{\nabla}^{-2}\hat{\nabla}^4)^{-1}\hat{\mathcal{B}}_{y,1}, \tag{A8e}$$

$$\mathcal{H}_{\nabla vz} = \hat{\nabla}\hat{\mathcal{C}}_{v,1}Re(\mathrm{i}\Omega\mathcal{I} - \hat{\nabla}^{-2}\hat{\nabla}^4)^{-1}\hat{\mathcal{B}}_{z,1}, \tag{A8f}$$

$$\mathcal{H}_{\nabla wx} = 0, \tag{A8g}$$

$$\mathcal{H}_{\nabla wy} = \hat{\nabla}\hat{\mathcal{C}}_{w,1}Re(\mathrm{i}\Omega\mathcal{I} - \hat{\nabla}^{-2}\hat{\nabla}^4)^{-1}\hat{\mathcal{B}}_{y,1}, \tag{A8h}$$

$$\mathcal{H}_{\nabla wz} = \hat{\nabla}\hat{\mathcal{C}}_{w,1}Re(\mathrm{i}\Omega\mathcal{I} - \hat{\nabla}^{-2}\hat{\nabla}^4)^{-1}\hat{\mathcal{B}}_{z,1}. \tag{A8i}$$

Applying the operation $\|\cdot\|_\infty = \sup_{\omega\in\mathbb{R}}\bar{\sigma}[\cdot] = \sup_{\Omega\in\mathbb{R}}\bar{\sigma}[\cdot]$, we have the scaling relation in theorem 4.1. ■

https://doi.org/10.1017/jfm.2021.762 Published online by Cambridge University Press

References

Balas, G., Chiang, R., Packard, A. & Safonov, M. 2005 Robust control toolbox. *For Use with Matlab. User's Guide, Version 3*.

Bamieh, B. & Dahleh, M. 2001 Energy amplification in channel flows with stochastic excitation. *Phys. Fluids* **13** (11), 3258–3269.

Barkley, D. 2016 Theoretical perspective on the route to turbulence in a pipe. *J. Fluid Mech.* **803**, P1.

Barkley, D. & Tuckerman, L.S. 2007 Mean flow of turbulent-laminar patterns in plane Couette flow. *J. Fluid Mech.* **576**, 109–137.

Bottin, S., Dauchot, O., Daviaud, F. & Manneville, P. 1998 Experimental evidence of streamwise vortices as finite amplitude solutions in transitional plane Couette flow. *Phys. Fluids* **10** (10), 2597–2607.

Brandt, L. 2014 The lift-up effect: the linear mechanism behind transition and turbulence in shear flows. *Eur. J. Mech. (*B*/Fluids)* **47**, 80–96.

Butler, K.M. & Farrell, B.F. 1992 Three-dimensional optimal perturbations in viscous shear flow. *Phys. Fluids* A **4** (8), 1637–1650.

Chapman, S.J. 2002 Subcritical transition in channel flows. *J. Fluid Mech.* **451**, 35–97.

Cherubini, S. & De Palma, P. 2013 Nonlinear optimal perturbations in a Couette flow: bursting and transition. *J. Fluid Mech.* **716**, 251–279.

Cherubini, S. & De Palma, P. 2015 Minimal-energy perturbations rapidly approaching the edge state in Couette flow. *J. Fluid Mech.* **764**, 572–598.

Chevalier, M., Hœpffner, J., Bewley, T.R. & Henningson, D.S. 2006 State estimation in wall-bounded flow systems. Part 2. Turbulent flows. *J. Fluid Mech.* **552**, 167–187.

De Souza, D., Bergier, T. & Monchaux, R. 2020 Transient states in plane Couette flow. *J. Fluid Mech.* **903**, A33.

Deguchi, K. & Hall, P. 2015 Asymptotic descriptions of oblique coherent structures in shear flows. *J. Fluid Mech.* **782**, 356–367.

Doyle, J. 1982 Analysis of feedback systems with structured uncertainties. *IEE Proc.* D-*Control Theory Appl.* **129** (6), 242–250.

Duguet, Y., Brandt, L. & Larsson, B.R.J. 2010*a* Towards minimal perturbations in transitional plane Couette flow. *Phys. Rev.* E **82** (2), 026316.

Duguet, Y., Monokrousos, A., Brandt, L. & Henningson, D.S. 2013 Minimal transition thresholds in plane Couette flow. *Phys. Fluids* **25** (8), 084103.

Duguet, Y. & Schlatter, P. 2013 Oblique laminar-turbulent interfaces in plane shear flows. *Phys. Rev. Lett.* **110** (3), 034502.

Duguet, Y., Schlatter, P. & Henningson, D.S. 2010*b* Formation of turbulent patterns near the onset of transition in plane Couette flow. *J. Fluid Mech.* **650**, 119–129.

Eckhardt, B., Schneider, T.M., Hof, B. & Westerweel, J. 2007 Turbulence transition in pipe flow. *Annu. Rev. Fluid Mech.* **39** (1), 447–468.

Ellingsen, T. & Palm, E. 1975 Stability of linear flow. *Phys. Fluids* **18** (4), 487–488.

Elofsson, P.A. & Alfredsson, P.H. 1998 An experimental study of oblique transition in plane Poiseuille flow. *J. Fluid Mech.* **358**, 177–202.

Farano, M., Cherubini, S., Robinet, J.C. & De Palma, P. 2015 Hairpin-like optimal perturbations in plane Poiseuille flow. *J. Fluid Mech.* **775**, R2.

Farano, M., Cherubini, S., Robinet, J.C. & De Palma, P. 2016 Subcritical transition scenarios via linear and nonlinear localized optimal perturbations in plane Poiseuille flow. *Fluid Dyn. Res.* **48** (6), 061409.

Farrell, B.F. & Ioannou, P.J. 1993 Stochastic forcing of the linearized Navier–Stokes equations. *Phys. Fluids* A **5** (11), 2600–2609.

Gustavsson, L.H. 1991 Energy growth of three-dimensional disturbances in plane Poiseuille flow. *J. Fluid Mech.* **224**, 241–260.

Hashimoto, S., Hasobe, A., Tsukahara, T., Kawaguchi, Y. & Kawamura, H. 2009 An experimental study on turbulent-stripe structure in transitional channel flow. In *Proceedings of the Sixth International Symposium on Turbulence Heat and Mass Transfer*. Rome.

Hœpffner, J., Chevalier, M., Bewley, T.R. & Henningson, D.S. 2005 State estimation in wall-bounded flow systems. Part 1. Perturbed laminar flows. *J. Fluid Mech.* **534**, 263–294.

Hof, B., Juel, A. & Mullin, T. 2003 Scaling of the turbulence transition threshold in a pipe. *Phys. Rev. Lett.* **91** (24), 244502.

Hwang, Y. & Cossu, C. 2010*a* Amplification of coherent streaks in the turbulent Couette flow: an input–output analysis at low Reynolds number. *J. Fluid Mech.* **643**, 333–348.

https://doi.org/10.1017/jfm.2021.762 Published online by Cambridge University Press

HWANG, Y. & COSSU, C. 2010*b* Linear non-normal energy amplification of harmonic and stochastic forcing in the turbulent channel flow. *J. Fluid Mech.* **664**, 51–73.
ILLINGWORTH, S.J. 2020 Streamwise-constant large-scale structures in Couette and Poiseuille flows. *J. Fluid Mech.* **889**, A13.
ILLINGWORTH, S.J., MONTY, J.P. & MARUSIC, I. 2018 Estimating large-scale structures in wall turbulence using linear models. *J. Fluid Mech.* **842**, 146–162.
JOVANOVIĆ, M. & BAMIEH, B. 2001 Modeling flow statistics using the linearized Navier–Stokes equations. In *Proceedings of the 40th IEEE Conference on Decision and Control*, pp. 4944–4949. IEEE.
JOVANOVIĆ, M.R. 2004 Modeling, analysis, and control of spatially distributed systems. PhD thesis, University of California at Santa Barbara.
JOVANOVIĆ, M.R. 2021 From bypass transition to flow control and data-driven turbulence modeling: an input-output viewpoint. *Annu. Rev. Fluid Mech.* **53** (1), 311–345.
JOVANOVIĆ, M.R. & BAMIEH, B. 2004 Unstable modes versus non-normal modes in supercritical channel flows. In *Proceedings of the 2004 American Control Conference*, pp. 2245–2250. IEEE.
JOVANOVIĆ, M.R. & BAMIEH, B. 2005 Componentwise energy amplification in channel flows. *J. Fluid Mech.* **534**, 145–183.
KALUR, A., MUSHTAQ, T., SEILER, P. & HEMATI, M.S. 2021*a* Estimating regions of attraction for transitional flows using quadratic constraints. *IEEE Control Syst. Lett.* **6**, 482–487.
KALUR, A., SEILER, P. & HEMATI, M.S. 2020 Stability and performance analysis of nonlinear and non-normal systems using quadratic constraints. *AIAA Scitech 2020 Forum*, p. 0833.
KALUR, A., SEILER, P. & HEMATI, M.S. 2021*b* Nonlinear stability analysis of transitional flows using quadratic constraints. *Phys. Rev. Fluids* **6** (4), 044401.
KANAZAWA, T. 2018 Lifetime and growing process of localized turbulence in plane channel flow. PhD thesis, Osaka University.
KERSWELL, R.R. 2018 Nonlinear nonmodal stability theory. *Annu. Rev. Fluid Mech.* **50** (1), 319–345.
KERSWELL, R.R., PRINGLE, C.C. & WILLIS, A.P. 2014 An optimization approach for analysing nonlinear stability with transition to turbulence in fluids as an exemplar. *Rep. Prog. Phys.* **77** (8), 085901.
KREISS, G., LUNDBLADH, A. & HENNINGSON, D.S. 1994 Bounds for threshold amplitudes in subcritical shear flows. *J. Fluid Mech.* **270**, 175–198.
LANDAHL, M.T. 1975 Wave breakdown and turbulence. *SIAM J. Appl. Maths* **28** (4), 735–756.
LIU, C. & GAYME, D.F. 2019 Convective velocities of vorticity fluctuations in turbulent channel flows: an input-output approach. In *Proceedings of the Eleventh International Symposium on Turbulence and Shear Flow Phenomenon, Southampton, UK*.
LIU, C. & GAYME, D.F. 2020*a* An input-output based analysis of convective velocity in turbulent channels. *J. Fluid Mech.* **888**, A32.
LIU, C. & GAYME, D.F. 2020*b* Input-output inspired method for permissible perturbation amplitude of transitional wall-bounded shear flows. *Phys. Rev.* E **102** (6), 063108.
LUNDBLADH, A., HENNINGSON, D.S. & REDDY, S.C. 1994 Threshold amplitudes for transition in channel flows. In *Transition, Turbulence and Combustion* (ed. M.Y. Hussaini, T.B. Gatski & T.L. Jackson), pp. 309–318. Springer.
MADHUSUDANAN, A., ILLINGWORTH, S.J. & MARUSIC, I. 2019 Coherent large-scale structures from the linearized Navier–Stokes equations. *J. Fluid Mech.* **873**, 89–109.
MCKEON, B.J. 2017 The engine behind (wall) turbulence: perspectives on scale interactions. *J. Fluid Mech.* **817**, P1.
MCKEON, B.J. & SHARMA, A.S. 2010 A critical-layer framework for turbulent pipe flow. *J. Fluid Mech.* **658**, 336–382.
MCKEON, B.J., SHARMA, A.S. & JACOBI, I. 2013 Experimental manipulation of wall turbulence: a systems approach. *Phys. Fluids* **25** (3), 031301.
MELLIBOVSKY, F. & MESEGUER, A. 2009 Critical threshold in pipe flow transition. *Phil. Trans. R. Soc. Lond.* A **367** (1888), 545–560.
MONOKROUSOS, A., BOTTARO, A., BRANDT, L., DI VITA, A. & HENNINGSON, D.S. 2011 Nonequilibrium thermodynamics and the optimal path to turbulence in shear flows. *Phys. Rev. Lett.* **106** (13), 134502.
MORRA, P., NOGUEIRA, P.A.S., CAVALIERI, A.V.G. & HENNINGSON, D.S. 2021 The colour of forcing statistics in resolvent analyses of turbulent channel flows. *J. Fluid Mech.* **907**, A24.
MULLIN, T. 2011 Experimental studies of transition to turbulence in a pipe. *Annu. Rev. Fluid Mech.* **43** (1), 1–24.
NOGUEIRA, P.A.S., MORRA, P., MARTINI, E., CAVALIERI, A.V.G. & HENNINGSON, D.S. 2021 Forcing statistics in resolvent analysis: application in minimal turbulent Couette flow. *J. Fluid Mech.* **908**, A32.

https://doi.org/10.1017/jfm.2021.762 Published online by Cambridge University Press

ORSZAG, S.A. 1971 Accurate solution of the Orr–Sommerfeld stability equation. *J. Fluid Mech.* **50** (4), 689–703.

PACKARD, A. & DOYLE, J. 1993 The complex structured singular value. *Automatica* **29** (1), 71–109.

PARANJAPE, C.S. 2019 Onset of turbulence in plane Poiseuille flow. PhD thesis, Institute of Science and Technology, Austria.

PARANJAPE, C.S., DUGUET, Y. & HOF, B. 2020 Oblique stripe solutions of channel flow. *J. Fluid Mech.* **897**, A7.

PEIXINHO, J. & MULLIN, T. 2007 Finite-amplitude thresholds for transition in pipe flow. *J. Fluid Mech.* **582**, 169–178.

PHILIP, J., SVIZHER, A. & COHEN, J. 2007 Scaling law for a subcritical transition in plane Poiseuille flow. *Phys. Rev. Lett.* **98** (15), 154502.

PRIGENT, A., GRÉGOIRE, G., CHATÉ, H. & DAUCHOT, O. 2003 Long-wavelength modulation of turbulent shear flows. *Physica* D **174** (1–4), 100–113.

PRIGENT, A., GRÉGOIRE, G., CHATÉ, H., DAUCHOT, O. & VAN SAARLOOS, W. 2002 Large-scale finite-wavelength modulation within turbulent shear flows. *Phys. Rev. Lett.* **89** (1), 014501.

PRINGLE, C.C.T. & KERSWELL, R.R. 2010 Using nonlinear transient growth to construct the minimal seed for shear flow turbulence. *Phys. Rev. Lett.* **105** (15), 154502.

PRINGLE, C.C.T., WILLIS, A.P. & KERSWELL, R.R. 2012 Minimal seeds for shear flow turbulence: using nonlinear transient growth to touch the edge of chaos. *J. Fluid Mech.* **702**, 415–443.

RABIN, S.M.E., CAULFIELD, C.P. & KERSWELL, R.R. 2012 Triggering turbulence efficiently in plane Couette flow. *J. Fluid Mech.* **712**, 244–272.

REDDY, S.C. & HENNINGSON, D.S. 1993 Energy growth in viscous channel flows. *J. Fluid Mech.* **252**, 209–238.

REDDY, S.C., SCHMID, P.J., BAGGETT, J.S. & HENNINGSON, D.S. 1998 On stability of streamwise streaks and transition thresholds in plane channel flows. *J. Fluid Mech.* **365**, 269–303.

REETZ, F., KREILOS, T. & SCHNEIDER, T.M. 2019 Exact invariant solution reveals the origin of self-organized oblique turbulent-laminar stripes. *Nat. Commun.* **10** (1), 2277.

REYNOLDS, O. 1883 XXIX. An experimental investigation of the circumstances which determine whether the motion of water shall be direct or sinuous, and of the law of resistance in parallel channels. *Phil. Trans. R. Soc. Lond.* **174**, 935–982.

ROMANOV, V.A. 1973 Stability of plane-parallel Couette flow. *Funct. Anal. Applics.* **7** (2), 137–146.

SAFONOV, M.G. 1982 Stability margins of diagonally perturbed multivariable feedback systems. *IEE Proc.* D-*Control Theory Appl.* **129** (6), 251–256.

SCHMID, P.J. 2007 Nonmodal stability theory. *Annu. Rev. Fluid Mech.* **39**, 129–162.

SCHMID, P.J. & HENNINGSON, D.S. 1992 A new mechanism for rapid transition involving a pair of oblique waves. *Phys. Fluids* A **4** (9), 1986–1989.

SCHMID, P.J. & HENNINGSON, D.S. 2001 *Stability and Transition in Shear Flows*. Springer Science & Business Media.

SHIMIZU, M. & MANNEVILLE, P. 2019 Bifurcations to turbulence in transitional channel flow. *Phys. Rev. Fluids* **4** (11), 113903.

SONG, B. & XIAO, X. 2020 Trigger turbulent bands directly at low Reynolds numbers in channel flow using a moving-force technique. *J. Fluid Mech.* **903**, A43.

SYMON, S., ILLINGWORTH, S.J. & MARUSIC, I. 2021 Energy transfer in turbulent channel flows and implications for resolvent modelling. *J. Fluid Mech.* **911**, A3.

TAO, J.J., ECKHARDT, B. & XIONG, X.M. 2018 Extended localized structures and the onset of turbulence in channel flow. *Phys. Rev. Fluids* **3** (1), 011902.

TILLMARK, N. & ALFREDSSON, P.H. 1992 Experiments on transition in plane Couette flow. *J. Fluid Mech.* **235**, 89–102.

TREFETHEN, L.N. 2000 *Spectral Methods in MATLAB*. SIAM.

TREFETHEN, L.N., TREFETHEN, A.E., REDDY, S.C. & DRISCOLL, T.A. 1993 Hydrodynamic stability without eigenvalues. *Science* **261** (5121), 578–584.

TSUKAHARA, T., SEKI, Y., KAWAMURA, H. & TOCHIO, D. 2005 DNS of turbulent channel flow at very low Reynolds numbers. In *Proceedings of the Fourth International Symposium on Turbulence and Shear Flow Phenomena, Williamsburg, USA*.

TUCKERMAN, L.S. & BARKLEY, D. 2011 Patterns and dynamics in transitional plane Couette flow. *Phys. Fluids* **23** (4), 041301.

TUCKERMAN, L.S., CHANTRY, M. & BARKLEY, D. 2020 Patterns in wall-bounded shear flows. *Annu. Rev. Fluid Mech.* **52** (1), 343–367.

https://doi.org/10.1017/jfm.2021.762 Published online by Cambridge University Press

TUCKERMAN, L.S., KREILOS, T., SCHROBSDORFF, H., SCHNEIDER, T.M. & GIBSON, J.F. 2014 Turbulent-laminar patterns in plane Poiseuille flow. *Phys. Fluids* **26** (11), 114103.

VADAREVU, S.B., SYMON, S., ILLINGWORTH, S.J. & MARUSIC, I. 2019 Coherent structures in the linearized impulse response of turbulent channel flow. *J. Fluid Mech.* **863**, 1190–1203.

WEIDEMAN, J.A.C. & REDDY, S.C. 2000 A MATLAB differentiation matrix suite. *ACM Trans. Math. Softw.* **26** (4), 465–519.

XIAO, X. & SONG, B. 2020 The growth mechanism of turbulent bands in channel flow at low Reynolds numbers. *J. Fluid Mech.* **883**, R1.

XIONG, X., TAO, J., CHEN, S. & BRANDT, L. 2015 Turbulent bands in plane-Poiseuille flow at moderate Reynolds numbers. *Phys. Fluids* **27** (4), 041702.

ZARE, A., JOVANOVIĆ, M.R. & GEORGIOU, T.T. 2017 Colour of turbulence. *J. Fluid Mech.* **812**, 636–680.

ZHOU, K., DOYLE, J.C. & GLOVER, K. 1996 *Robust and Optimal Control*. Prentice Hall.

https://doi.org/10.1017/jfm.2021.762 Published online by Cambridge University Press